


Identification of diverse lipid-binding modes in the groove of zinc α_2 glycoprotein reveals its functional versatility

Henna Zahid¹, Andy M. Lau¹, Sharon M. Kelly², Kersti Karu³, Jayesh Gor¹, Stephen J. Perkins¹ and Lindsay C. McDermott⁴ 

¹ Department of Structural and Molecular Biology, University College London, UK

² Institute of Molecular, Cell and Systems Biology, College of Medical, Veterinary and Life Sciences, University of Glasgow, UK

³ Department of Chemistry, University College London, UK

⁴ School of Life Sciences, University of Bedfordshire, Luton, UK

Keywords

fatty acids; fluorescence; MHC; signalling lipids; zinc α_2 glycoprotein

Correspondence

L. C. McDermott, School of Life Sciences, University of Bedfordshire, Park Square, Luton LU1 3JU, UK

Tel: +44 (0)1582 489 644

E-mail: lindsay.mcdermott@beds.ac.uk

(Received 19 April 2021, revised

3 November 2021, accepted 22 November 2021)

doi:10.1111/febs.16293

ZAG is a multifunctional glycoprotein with a class I MHC-like protein fold and an α_1 - α_2 lipid-binding groove. The intrinsic ZAG ligand is unknown. Our previous studies showed that ZAG binds the dansylated C₁₁ fatty acid, DAUDA, differently to the boron dipyrromethane C₁₆ fatty acid, C₁₆-BODIPY. Here, the molecular basis for this difference was elucidated. Multi-wavelength analytical ultracentrifugation confirmed that DAUDA and C₁₆-BODIPY individually bind to ZAG and compete for the same binding site. Molecular docking of lipid-binding in the structurally related Cluster of differentiation 1 proteins predicted nine conserved ligand contact residues in ZAG. Twelve mutants were accordingly created by alanine scanning site directed mutagenesis for characterisation. Mutation of Y12 caused ZAG to misfold. Mutation of K147, R157 and A158 abrogated C₁₆-BODIPY but not DAUDA binding. L69 and T169 increased the fluorescence emission intensity of C₁₆-BODIPY but not of DAUDA compared to wild-type ZAG and showed that C₁₆-BODIPY binds close to T169 and L69. Distance measurements of the crystal structure revealed K147 forms a salt bridge with D83. A range of bioactive bulky lipids including phospholipids and sphingolipids displaced DAUDA from the ZAG binding site but unexpectedly did not displace C₁₆-BODIPY. We conclude that the ZAG α_1 - α_2 groove contains separate but overlapping sites for DAUDA and C₁₆-BODIPY and is involved in binding to a bulkier and wider repertoire of lipids than previously reported. This work suggested that the *in vivo* activity of ZAG may be dictated by its lipid ligand.

Introduction

Zinc α_2 glycoprotein (ZAG) is a 42 kDa multifunctional glycoprotein which is ubiquitously expressed in a range of tissues [1,2]. It is a secreted soluble protein first isolated from human plasma in 1961 [3] and further identified in saliva, sweat, milk and prostatic

fluid [4]. Its most well described function is as an adipokine and controller of body weight. Indeed, addition of ZAG to murine adipocytes stimulated lipolysis [5]. Similarly, treatment of ob/ob mice with ZAG reduced their fat stores [5]. ZAG knock out mice gained weight

Abbreviations

AUC, analytical ultracentrifugation; C₁₆-BODIPY, 4,4-difluoro-5,7-dimethyl-4-bora-3a,4a-diaza-s-indacene-3-hexadecanoic acid; CD, circular dichroism; DAUDA, 11-[5-(dimethylamino)-1-naphthalenesulfonylamino] undecanoic acid; K_d, dissociation constant; MHC, major histocompatibility complex; PBS, phosphate buffered saline; PEG, polyethylene glycol; Wt, wild-type; ZAG, zinc α_2 glycoprotein.

when fed a lipid-rich diet [6] while overexpression of ZAG in mice reduced their fat stores [7]. Expression of ZAG in adipocytes was inversely correlated with fat mass [8,9] and adipocyte secreted ZAG was found to act locally in lipolysis [10]. Furthermore, ZAG interacted with β_2 and β_3 adrenergic receptors [11] to induce lipolysis in mice, although the role of ZAG as a typical β_2 and β_3 adrenergic receptor agonist has been debated [12]. ZAG promoted browning of white adipose tissue [13,14] and recently, amine oxidase copper-containing three was identified as a binding partner for ZAG [15]. ZAG inhibited its activity, and stimulated lipolysis [15]. ZAG has further been reported to have roles in sperm motility [16,17], cell adhesion [18], melanin production [19] and tumour proliferation [20]. ZAG is dysregulated in cancer [21–23] and a range of inflammatory diseases [24–27]. The molecular mechanisms underlying the functions of ZAG and its roles in the diseases in which it is dysregulated are not known.

The first crystal structure of ZAG revealed a class I major histocompatibility complex (MHC) fold with an α_1 - α_2 groove containing a region of unidentified electron density (Fig. 1) [28]. Peptides are typically bound by class I MHC proteins [29]. Subsequent biochemical studies however revealed that the unidentified ligand in ZAG was not a peptide [30]. Nine hydrophobic and one charged residues (I76, F77, W115, W134, W148, Y14, Y117, Y154, Y161 and R73), surrounded the area of unidentified electron density in the first ZAG crystal structure [28]. A collection of hydrophobic residues and a single arginine are typically used to bind fatty acids in intracellular fatty acid binding proteins [31]. Indeed ZAG was shown to bind the fluorescently tagged ligand DAUDA with a micromolar dissociation constant (Fig. 1) [32]. DAUDA fluorescence displacement assays showed that ZAG had a preference for long chain polyunsaturated fatty acids [32]. Crystallographic and fluorescence studies revealed that the unidentified electron density in the ZAG crystal

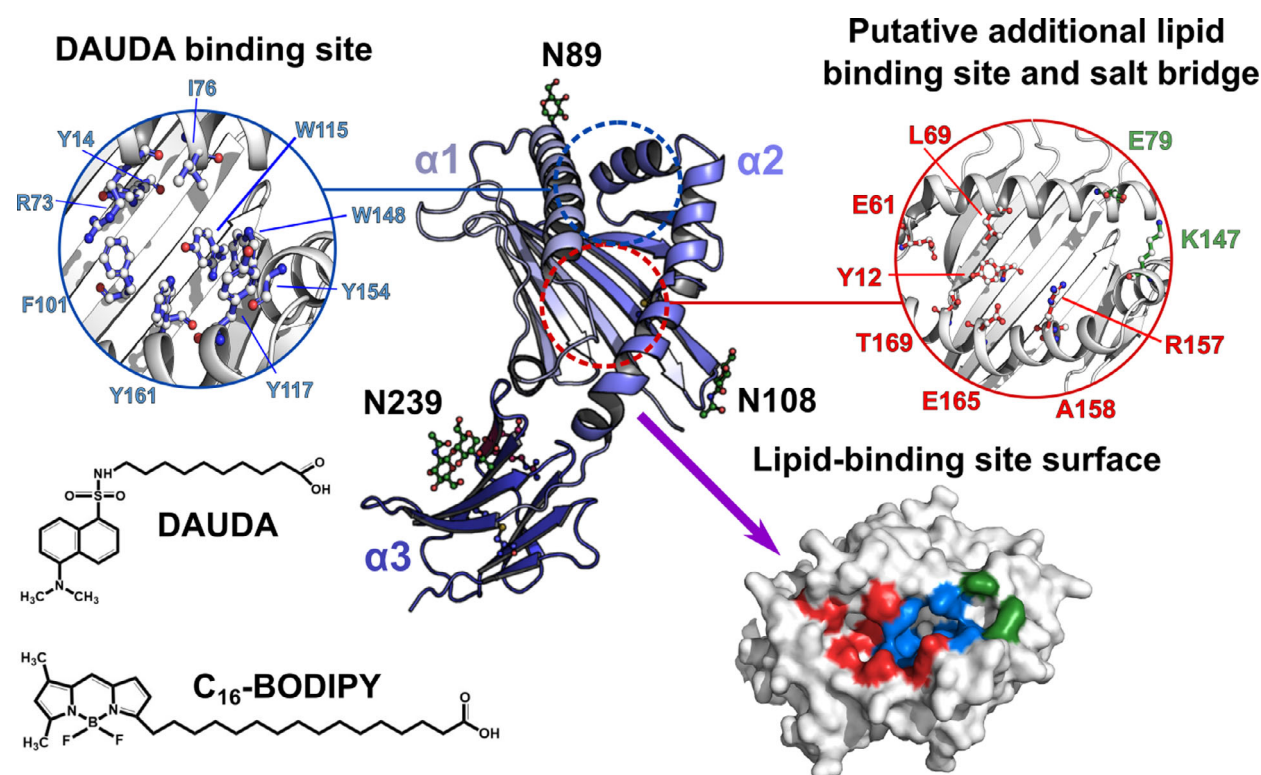


Fig. 1. Observed and putative lipid binding sites of Wt ZAG. Centre: Cartoon representation of the secondary structure of ZAG (PDB ID: 1ZAG). The α_1 domain is shown in lilac, α_2 in light blue and the α_3 domain in navy. Three glycosylation sites at N89, N106 and N239 are shown in green. Bottom left: The chemical structures of DAUDA and C_{16} -BODIPY are shown. Bottom right: Surface representation of the ZAG groove showing the location of DAUDA (blue), other potential lipid-binding residues (red) and a hypothesized salt bridge (green). Top right: Seven residues predicted to form an additional lipid binding site (no ligand is shown), together with the E79-K147 salt bridge, are shown. Top left: Nine residues identified by mutagenesis and crystallography to form the DAUDA binding site are shown. Protein structures were created using the PyMOL Molecular Graphics System, Version 2.5, Schrödinger, LLC.

structure was polyethylene glycol (PEG), a precipitant used to crystallise proteins and that the DAUDA and PEG binding sites were coincident [33]. Alanine scanning site directed mutagenesis studies that targeted ten residues I76, F77, W115, W134, W148, Y14, Y117, Y154, Y161 and R73 in the ZAG groove further confirmed the location of the DAUDA binding site in ZAG and identified Y14, F77, I76, Y154, Y161 and R73 as crucial for DAUDA binding [34]. The boron dipyrromethene fatty acid, C₁₆-BODIPY, was also shown to bind to ZAG (Fig. 1) [35]. In the presence of increasing concentrations of Zn²⁺, ZAG oligomerised [35]. Recombinant *E. coli* ZAG contained one tight and fifteen loose zinc binding sites, the latter thought to be responsible for the precipitation of ZAG from human plasma during its purification [36]. ZAG-Zn²⁺ oligomers showed reduced C₁₆-BODIPY and similar DAUDA binding when compared with *apo* ZAG [35]. Collectively, these findings suggested the presence of two distinct fatty acid binding sites in ZAG, similar to that observed in Cluster of differentiation-1c (CD1c), an immune class I MHC protein, which binds several bacterial lipid-based antigens for recognition by T-cells [37]. Recently, the first crystal structure of ZAG bound to DAUDA was solved [38]. This revealed that the ZAG α 1- α 2 groove was flexible and able to accommodate DAUDA in two different positions in the ZAG groove. The first position was the previously described DAUDA binding site [34,38] and the second was close to a different site in the ZAG groove (Fig. 1) [38].

The identity of ZAG's physiological lipid ligand is unknown, yet this information is essential to understand both how ZAG functions and becomes dysregulated in disease. To clarify the molecular basis of lipid binding to ZAG, here, we explored the binding of DAUDA and C₁₆-BODIPY to ZAG using the recently developed multi-wavelength Optima analytical ultracentrifuge (AUC), followed by site directed mutagenesis that was informed by *in silico* docking analyses. Using fluorescence displacement assays, we further screened a range of bulky lipid ligands including phospholipids, diacyl glycerol and a very long chain fatty acid for binding to ZAG. Our results showed that the DAUDA and C₁₆-BODIPY binding sites in ZAG are indeed separate but overlapping. Furthermore, bulky lipids were unable to displace C₁₆-BODIPY but were able to displace DAUDA from ZAG. Taken together, our results revealed that the whole ZAG groove is active in lipid binding and can accommodate a broader range of signalling lipids than previously thought. We conclude that the *in vivo* function of ZAG may therefore be dictated by its bound lipid.

Results

Multiple wavelength AUC of ZAG

To study the binding of DAUDA and C₁₆-BODIPY to Wt ZAG in PBS, a multi-wavelength Optima AUC instrument was used with ZAG. The absorbance profiles of DAUDA and C₁₆-BODIPY produced maxima at 335 and 505 nm respectively. The AUC signal at 335 nm was used to track the sedimentation of DAUDA in complex with ZAG, and that at 515 nm was used to track C₁₆-BODIPY in complex with ZAG. Because the ZAG:C₁₆-BODIPY samples gave more intense signals at 505 nm, data at 515 nm were used to prevent saturation of the AUC detector. A wavelength of 280 nm was used to track ZAG in the absence and presence of DAUDA or C₁₆-BODIPY. Experimental boundary scans were well fitted at each wavelength for *apo* Wt-ZAG (Fig. 2A), and the 1 : 1 ZAG: DAUDA (Fig. 2C,D) and 1 : 1 ZAG: C₁₆-BODIPY complexes (Fig. 2F,G). The size-distribution $c(s)$ plot for *apo* Wt-ZAG produced a single monomeric peak at 2.72 ± 0.93 S (Fig. 2B), in close agreement to previously reported values of 2.83 ± 0.02 S and 2.67 ± 0.01 S [35], and corresponded to a molecular mass of 31 000 Da. The size-distribution $c(s)$ plot for 1 : 1 ZAG: DAUDA produced a single monomeric peak at 2.71 ± 0.95 S (280 nm) and 2.70 ± 0.04 S, (335 nm), respectively (Fig. 2E). For ZAG:DAUDA, these results agreed with those previously measured in PBS, although low amounts of tetramer were seen previously at 6.4 S in 20 mM Hepes buffer, pH 7.6 but not for PBS [38]. The $c(s)$ plot for 1 : 1 ZAG: C₁₆-BODIPY produced a single monomeric peak at 2.73 ± 0.94 S (280 nm) and 2.89 ± 0.16 S (515 nm), respectively (Fig. 2H). Thus, DAUDA and C₁₆-BODIPY each individually bind to ZAG during the AUC runs as expected.

To determine if the binding of DAUDA and C₁₆-BODIPY to ZAG was competitive or non-competitive, the sedimentation profiles and $c(s)$ plots of three ZAG:DAUDA:C₁₆-BODIPY complexes were examined. As the benchmark, the fitted experimental boundary scans for a 1 : 1 : 1 ZAG:DAUDA:C₁₆-BODIPY complex (Fig. 3A–C) yielded $c(s)$ plots containing monomeric peaks at 2.60 ± 1.09 S (280 nm), 2.67 ± 0.04 S (335 nm) and 2.86 ± 0.08 S (515 nm; Fig. 3D,E). In addition, smaller peaks were seen at 4 S (335 nm; ~ 40%) and 5 S (515 nm; ~ 10%) corresponding to approximately dimeric molecular masses of 68 300 Da (Fig. 3E). This outcome showed that DAUDA and C₁₆-BODIPY were both bound to ZAG at equimolar ligand concentrations and caused ZAG

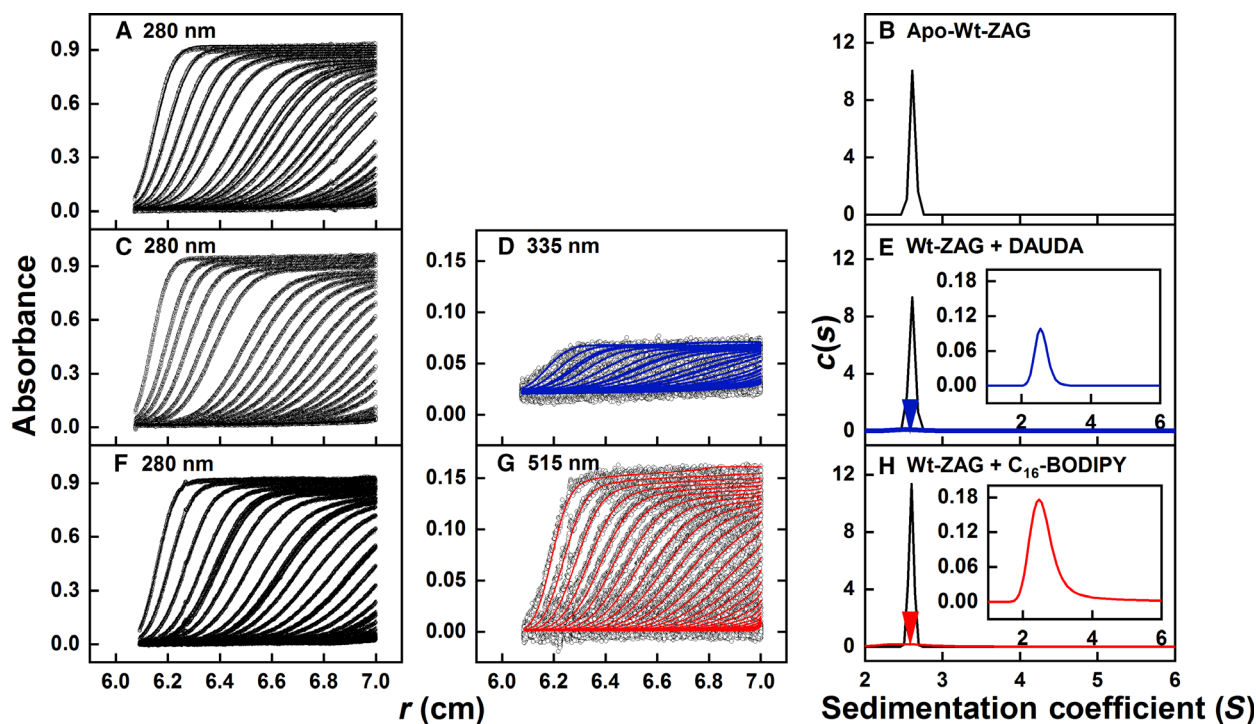


Fig. 2. Size-distribution analyses $c(s)$ of Wt ZAG and its complexes with DAUDA and C_{16} -BODIPY. The concentration of Wt ZAG was $11 \mu\text{M}$ in PBS pH 7.4 in all runs. The ratios of each species for Wt ZAG:DAUDA: C_{16} -BODIPY were (A) 1 : 0 : 0 (C) 1 : 1 : 0 (F) 1 : 0 : 1, respectively. The resulting size-distribution $c(s)$ analyses of (A) are shown in (B) for 280 nm only, (C, D) in (E) for 280 nm (black) and 335 nm (blue), and (F, G) in (H) for 280 nm (black) and 515 nm (red).

to form small or trace amounts of dimer. To reveal whether these two ligands bound competitively, a five-fold excess of C_{16} -BODIPY was first used. The maximum absorbance value for the fitted experimental boundary scans at 335 nm of the 1 : 1 : 5 ZAG : DAUDA : C_{16} -BODIPY complex decreased to 0.04 (Fig. 3G), compared with 0.06 for the equimolar complex (Fig. 3B). Monomeric peaks at 2.6 S were again seen at all wavelengths in the $c(s)$ plots, and additional smaller dimer peaks were observed at 4.5 S (335 nm; 16%) and 5.3 S (515 nm; 7%) corresponding to approximate dimer molecular weights (Table 1, arrowed in Fig. 3J). Excess C_{16} -BODIPY therefore partially displaced DAUDA in ZAG. Next, in the presence of a five-fold excess of DAUDA, the maximum absorbance value for the fitted experimental boundary scans at 515 nm of the 1 : 5 : 1 ZAG: DAUDA: C_{16} -BODIPY complex decreased to 0.045 (Fig. 3M) compared to a value of 0.15 for the equimolar complex (Fig. 3C). Monomeric peaks were again seen at all wavelengths in the $c(s)$ plots and a trace dimer peak was observed at 5.56 ± 0.01 S (515 nm; 2%; Table 1, Fig. 3N,O). Excess DAUDA therefore displaced C_{16} -BODIPY in ZAG. Taken together, these three sets of AUC results indicate that ZAG contains

coincident binding sites for DAUDA and C_{16} -BODIPY in which the ligands competed with each other.

Molecular docking

To examine the molecular properties of the ZAG groove, a total of 20 hydrophobic ligands identified from CD1a-CD1d crystal structures were docked with the ZAG groove using AutoDock Vina. The ligands included alkanes (C_6 , C_{12} , C_{22} , C_{24}), saturated C_{11} and C_{16} fatty acids, monounsaturated C_{18} fatty acids, glycolipids and phospholipids varying in chain length from C_8 to C_{50} , gangliosides and lipopeptides (Table S1). Analysis of the docked protein-ligand complexes using LIGPLOT software identified 20 ZAG residues, which made contacts with > 25% of the 20 ligands (Fig. 4A). Eleven of these 20 residues corresponded to the previously identified DAUDA binding pocket (Y14, R73, I76, F77, F101, W115, Y117, W134, W148, Y154 and Y161; [34]), all of which were fully conserved across eight primate, two murine and one bovine ZAG sequences (blue, Fig. 4B). Mapping these 20 identified residues to the ZAG groove resulted in the prediction of nine residues (red, Fig. 4B) that were additional to

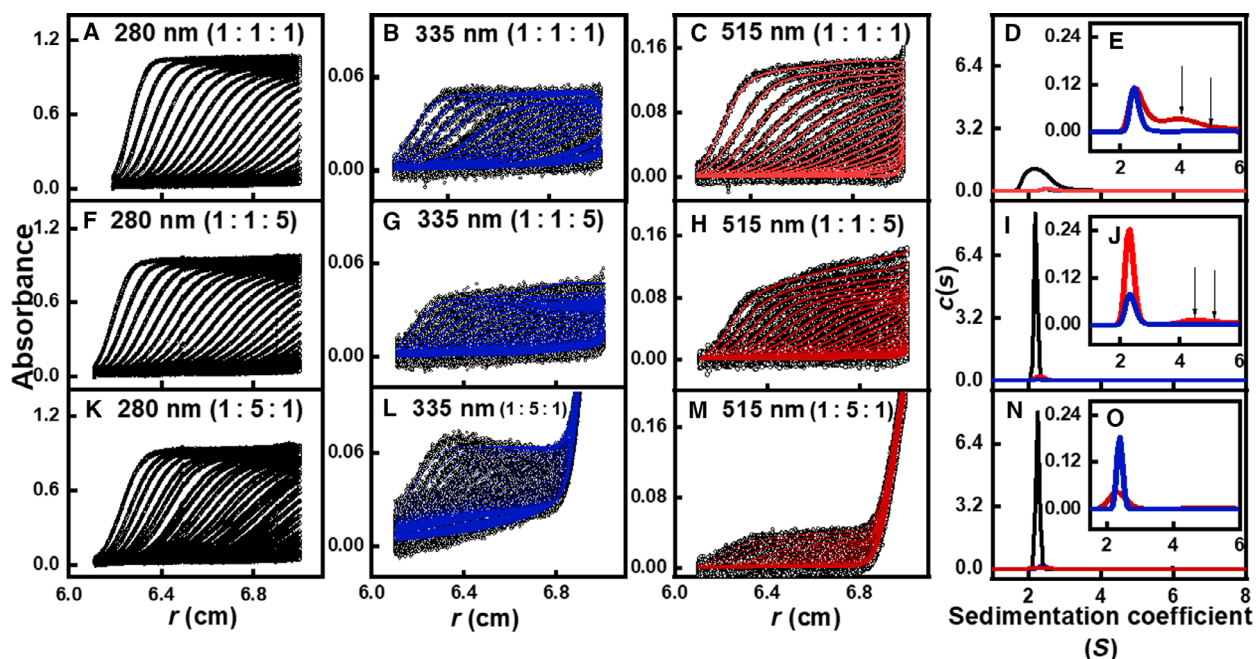


Fig. 3. Multiwavelength AUC size-distribution analyses $c(s)$ of DAUDA and C_{16} -BODIPY binding to Wt ZAG at different molar ratios. In the nine panels showing the boundary fits, the molar ratios of each species are indicated in brackets to correspond to ZAG:DAUDA: C_{16} -BODIPY. Sedimentation boundary fits of equimolar ratios of Wt ZAG, DAUDA and C_{16} -BODIPY are shown at (A) 280 nm (black), (B) 335 nm (blue) and (C) 515 nm (red). In (D,E), the resulting $c(s)$ distribution of equimolar Wt ZAG (black), DAUDA (inset, blue) and C_{16} -BODIPY (inset, red) are shown. The arrows denote the position of small dimer peaks. For the 1 : 1 : 5 ratio, the boundary fits observed at 280 nm, 335 nm and 515 nm are shown in (F–H). The resulting $c(s)$ distributions are shown in (I, J). For the 1 : 5 : 1 ratio, the boundary fits observed at 280 nm, 335 nm and 515 nm are shown in (K–M). The resulting $c(s)$ distributions are shown in (N, O).

Table 1. The $s_{20,w}$ values from sedimentation velocity analyses of apo ZAG and the ZAG:DAUDA: C_{16} -BODIPY binary and ternary complexes. Sedimentation data were collected from ZAG:lipid mixtures centrifuged at 50 000 rpm at different wavelengths: 280 nm to track ZAG, 335 nm to track DAUDA and 515 nm to track C_{16} -BODIPY. The sedimentation data were used to produce individual $c(s)$ plots yielding $s_{20,w}$ (S) values for the different ZAG:lipid mixtures. Small peaks of $s_{20,w}$ values were not considered. NA, not available.

Protein-ligand	$s_{20,w}$ (S)		
	280 nm	335 nm	515 nm
ZAG	2.72 ± 0.93	NA	NA
ZAG:DAUDA (1 : 1)	2.71 ± 0.95	2.70 ± 0.04	NA
ZAG: C_{16} -BODIPY (1 : 1)	2.73 ± 0.94	NA	2.89 ± 0.16
ZAG:DAUDA: C_{16} -BODIPY (1 : 1 : 1)	2.6 ± 1.09	2.67 ± 0.04	2.86 ± 0.08
ZAG:DAUDA: C_{16} -BODIPY (1 : 1 : 5)	2.47 ± 0.96	2.62 ± 0.03	2.63 ± 0.08
ZAG:DAUDA: C_{16} -BODIPY (1 : 5 : 1)	2.40 ± 1.00	2.55 ± 0.04	2.52 ± 0.01

our 2006 study (33) that were potentially involved in fatty acid binding and located in close proximity to the DAUDA binding site: Y12, E61, L69, E79, K147, R157, A158, E165 and T169 (Fig. 1). Seven of these (Y12, E61, L69, R157, A158, E165 and T169) were located to the left of the previously identified DAUDA binding site (Fig. 1). It was therefore hypothesised that these seven residues represented part of a larger lipid binding site in the ZAG groove, and possibly for C_{16} -BODIPY. The remaining two residues E79 and K147

were located beside the DAUDA binding site close to each other but far from the predicted second fatty acid binding site (Fig. 1). K147 was fully conserved across all species in the ZAG sequence alignment, although an E79Q substitution was observed in the white-tufted-ear marmoset sequence (UniProt: F6W5A5). These oppositely charged E79 and K147 residues may interact to form a salt bridge. All nine additional residues identified from *in silico* screening were therefore selected for mutagenesis studies.

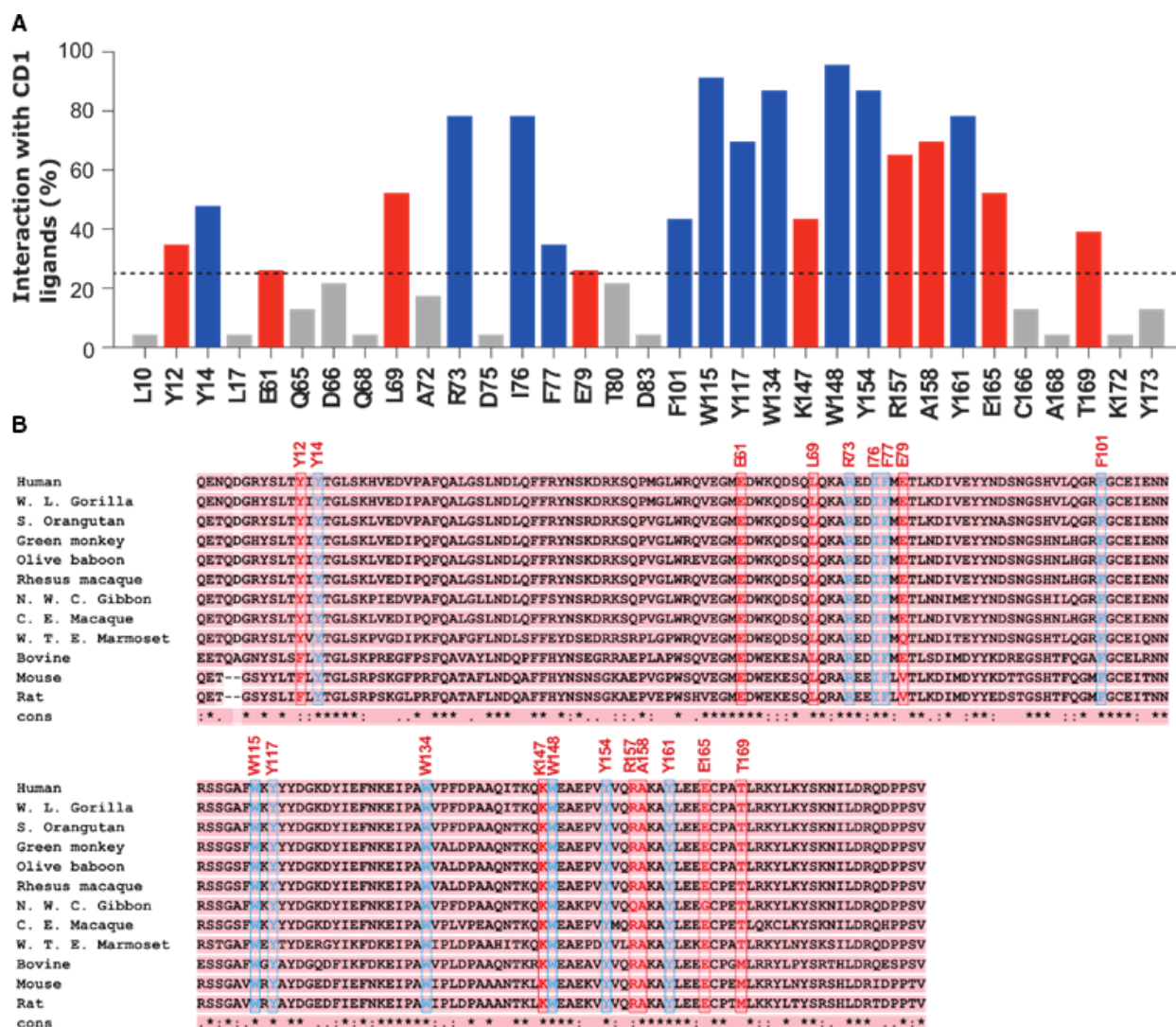


Fig. 4. Predicted ligand interacting residues of ZAG from molecular docking. (A) Percentage of interaction between individual residues with the total number of docked ligands. The ZAG groove was docked with ligands ($n = 20$) extracted from crystal structures of CD1a-d. LIGPLOT software was used to identify interacting ZAG residues within 4 Å of the ligand (Table S1). Residues of interest were identified as those with an interaction percentage greater than 25% (dotted line). Nine new putative groove binding residues identified from the docking analysis are highlighted in red here and below. Residues known to interact with DAUDA are shown in blue here and below. (B) Multiple sequence alignment of human ZAG with ZAG in 11 other species (Materials and Methods). The 'cons' represents the residue conservation score, where colon ':', period '.' and asterisk '*', denote size, property and full conservation.

Expression and purification differences between Wt and mutant ZAG

Together with Wt ZAG, 12 mutant ZAG pET-23a constructs were prepared (Materials and methods). These included constructs for Y12A, E61A, L69A, E79A, K147A, R157A, R157E, A158G, E165A and T169A, and also R73A and R73E as negative controls. Previous studies showed that the mutation of R73 altered the structure of ZAG and abolished DAUDA

binding [34]. Following transformation of mutant ZAG constructs into BL21(DE3)pLysE cells, Wt and mutant proteins were individually expressed and purified by size-exclusion chromatography following the refolding of denatured inclusion bodies. The elution times of Wt and mutant ZAG proteins clustered into three groups: the Wt ZAG and three mutants (R157E, E79A and Y12A) eluted at ~90 mL and produced a single peak (Fig. 5A); six mutants (R73A, E61A, L69A, R157A, R73E and K147A) eluted slightly

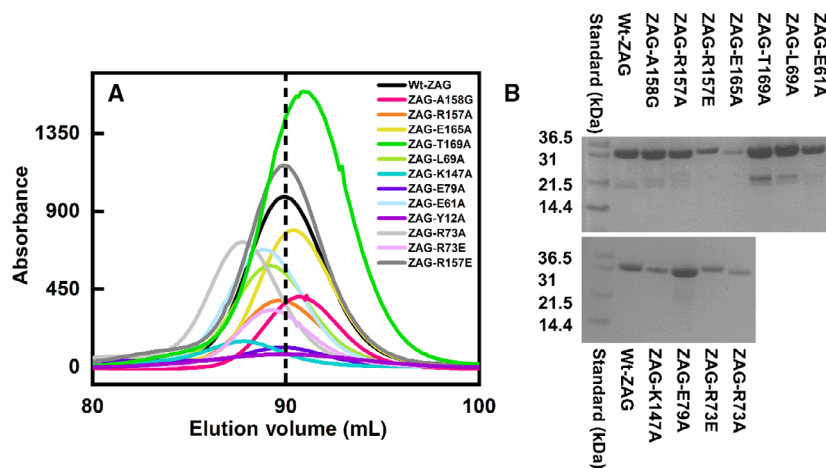


Fig. 5. Purification Wt and mutant ZAG. (A) Size exclusion chromatograms for Wt ZAG (black) and 12 ZAG-mutants: A158G (pink), R157A (orange), E165A (yellow), T169A (green), L69A (light green), K147A (blue), E79A (dark purple), E61A (light blue), Y12A (purple), R73A (light grey), R73E (lilac), R157E (dark grey). The vertical dotted black line represents the Wt ZAG elution volume for comparison. (B) Non-reducing 4–12% SDS-PAGE analysis of Wt and 11 ZAG mutants (i.e. excluding ZAG-Y12A). All protein concentrations used were between 2 and 8 μM .

earlier, while three mutants (T169A, E165A and A158G) eluted slightly later. These differences in elution volumes suggested there may be small differences in the solution properties of the ZAG mutants in comparison to the Wt type. The yield of each ZAG mutant as determined by A_{280} absorbance readings was varied. Wt ZAG gave a yield of 2.9 $\text{mg}\cdot\text{L}^{-1}$ of bacterial culture, and R73E, R157A and A158G mutants gave comparable yields of 2.4–4.2 $\text{mg}\cdot\text{L}^{-1}$ culture. A second group of mutants gave yields in the range of 1.0–1.9 $\text{mg}\cdot\text{L}^{-1}$ culture (R157E, E79A, L69A, T169A and E165A). Three mutants (K147A, E61A and R73A) gave lower yields of 0.6–0.9 $\text{mg}\cdot\text{L}^{-1}$ culture, while the Y12A mutant was consistently lower at 0.23 $\text{mg}\cdot\text{L}^{-1}$ culture, and was therefore not analysed by SDS-PAGE. The remaining mutant proteins and Wt type ZAG revealed single protein bands at an apparent molecular mass of ~ 32 kDa on 4%–12% non-reducing SDS-PAGE in keeping with the theoretical molecular mass of each protein, with some other protein traces at ~ 21 kDa in two overloaded wells (Fig. 5B and Fig. S1). Overall, Wt ZAG and the 12 mutant proteins were mostly purified to apparent homogeneity.

Near and far-UV CD of Wt and mutant ZAG

The tertiary and secondary structures of Wt and mutant ZAG were analysed by near and far-UV CD to determine if any of the mutations had induced structural changes. The correct folding of ZAG and mutant proteins was monitored by examining two maxima at 265 and 290 nm and a minimum at 285 nm in the near-UV spectra of Wt and mutant ZAG proteins, and a maximum and minimum at 190 and 220 nm in the far-UV spectra. The near-UV spectrum of Wt ZAG showed a maximum at 265 nm, likely to

correspond to disulphide chromophores and phenylalanine residues (Fig. 6A) [39]; Wt ZAG contains four cysteines, which form two pairs of disulphides; C103-C166 in the $\alpha 1$ - $\alpha 2$ ZAG groove and C205-C260 in the $\alpha 3$ domain and nine phenylalanine residues. A tryptophan peak at 290 nm and tyrosine minimum at 285 nm were present in the near-UV spectrum of Wt ZAG (Fig. 6A). Wt ZAG contains eight tryptophan and 18 tyrosine residues. The far-UV spectrum of Wt ZAG displayed a positive maximum at 190 nm, and a negative minimum at 218 nm, which were attributed to α -helices and β -pleated sheets (Fig. 6B). These observations agreed with previous near and far-UV CD measurements of Wt ZAG and confirmed its correct folding [34]. Of the 12 ZAG-mutants, ten showed no significant distortion in the spectral shape or intensity in the far-UV CD region (corresponding to secondary structure) and only moderate differences in the intensities in the near-UV CD regions (corresponding to environment of the aromatic and disulphide residues) in comparison to the Wt protein (Fig. 6A,B). In contrast, the near-UV spectrum of the Y12A mutant revealed a notable reduction of the 265 nm peak and lacked the tyrosine minimum and tryptophan peak at 285 and 290 nm, respectively. In the far-UV CD, the overall shape of the ZAG-Y12A spectrum was significantly different. Thus, the secondary and tertiary structures of Y12A were perturbed, and Y12A was used below as a control for misfolded ZAG. ZAG-R73A also displayed altered near and far UV spectra in comparison to Wt ZAG (Fig. 6A,B) to suggest that the secondary and tertiary structures were affected by the mutation (Fig. 6A,B). It was concluded that residues Y12 and R73 were key for the integrity of the ZAG secondary and tertiary structures.

AUC of Wt and mutant ZAG

AUC sedimentation velocity experiments were performed to determine the mass, shape and oligomeric state of each of the Wt and mutant ZAG proteins. The mass and shape of a protein is encapsulated by its sedimentation coefficient $s_{20,w}$ value, which is obtained from a size distribution analysis based on the sedimentation boundaries of the protein in the AUC experiment and subsequent $c(s)$ plot [40]. Oligomers would have increased $s_{20,w}$ values. Absorbance AUC data sets were collected for each protein and the sedimentation boundaries were well fitted in the resulting $c(s)$ size distribution analyses (Fig. S2A–C). Analyses of these data sets produced size distribution $c(s)$ plots for all 13 proteins (Fig. S2D–N). In agreement with previous findings, Wt ZAG produced a single monomeric peak

with a $s_{20,w}$ value of 2.67 ± 0.01 S (Fig. S2D) [35]. Mass distribution analysis $c(M)$ showed that the monomeric Wt ZAG peak corresponded to a molecular mass of 30.2 kDa, which agreed with the canonical native sequence-derived value of 32 kDa. All the ZAG mutants except for Y12A were found to be monomeric with $s_{20,w}$ values ranging between 2.31 and 2.89 S (Fig. S2E–N). In line with the aberrant CD curves observed in the previous section (Fig. 6), Y12A produced two peaks at 3.47 S and 4.62 S indicating the presence of both monomer and dimer (Fig. S2N). In conclusion, AUC sedimentation velocity experiments revealed that the Wt and 11 of the 12 mutants were folded monomers, with the exception of Y12A.

Fluorescence ligand binding assays of Wt and mutant ZAG

In order to locate the C₁₆-BODIPY binding site in ZAG, we performed a series of fluorescence ligand binding assays using Wt ZAG and 12 ZAG mutants. In these assays, the fluorescence emission spectra of C₁₆-BODIPY is monitored as a function of increasing ZAG concentration. The fluorescence intensity of C₁₆-BODIPY increases in a hydrophobic environment and exhibits a red spectral shift [35,41]. For Wt ZAG, a sequential addition of nine doses at 0.24 μM each, into 1.3 μM C₁₆-BODIPY, resulted in a sequential increase in the fluorescence emission intensity to saturation and a red shift in the maximum emission wavelength from 511 to 519 nm to show that C₁₆-BODIPY binds to ZAG (Fig. 7B). In addition, we derived from the assay, a dissociation constant (K_d) of 0.16 ± 0.09 μM for this interaction, in agreement with our previous value of 0.06 ± 0.01 μM [35] (Fig. 7F and Table 2).

Following this methodology, we performed titrations of the 12 ZAG mutants with C₁₆-BODIPY. Each assay was monitored for changes in the emission wavelength, K_d value and fluorescence emission intensity. Firstly, like Wt ZAG, the six A158G, R157A, E165A, T169A, L69A and E61A mutants produced similar red shifts in their fluorescence emission wavelengths from 511 to 519 nm (Fig. 7D; Figs S3 and S4). This indicated that these six mutated residues had not perturbed the C₁₆-BODIPY binding site in ZAG. E79A produced a red shift from 511 to 520 nm, again indicating that mutation of this residue did not significantly perturb the C₁₆-BODIPY binding site in ZAG. Smaller red shifts from 511 to 517 nm were seen for K147A, and from 511 to 514 nm for Y12A, R157E and R73A (Fig. 7D, Figs S4 and S5) and indicated that the C₁₆-BODIPY ZAG binding site had been perturbed by these four mutations. R73E induced a negligible shift in the C₁₆-

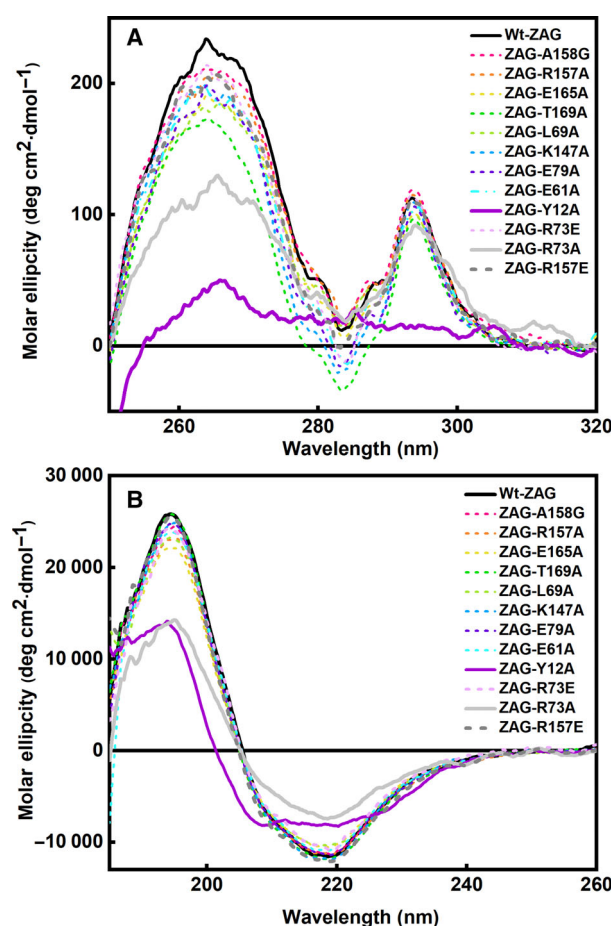


Fig. 6. Secondary and tertiary structures of Wt and mutant ZAG by CD spectroscopy. (A) Near-UV and (B) far-UV CD analysis of Wt and ZAG-mutants. All proteins were measured within a concentration range of 0.1–0.5 mg·mL⁻¹, in 50 mM Na₂HPO₄, pH 7.4. All scans were corrected for pathlength, protein concentration and buffer contribution.

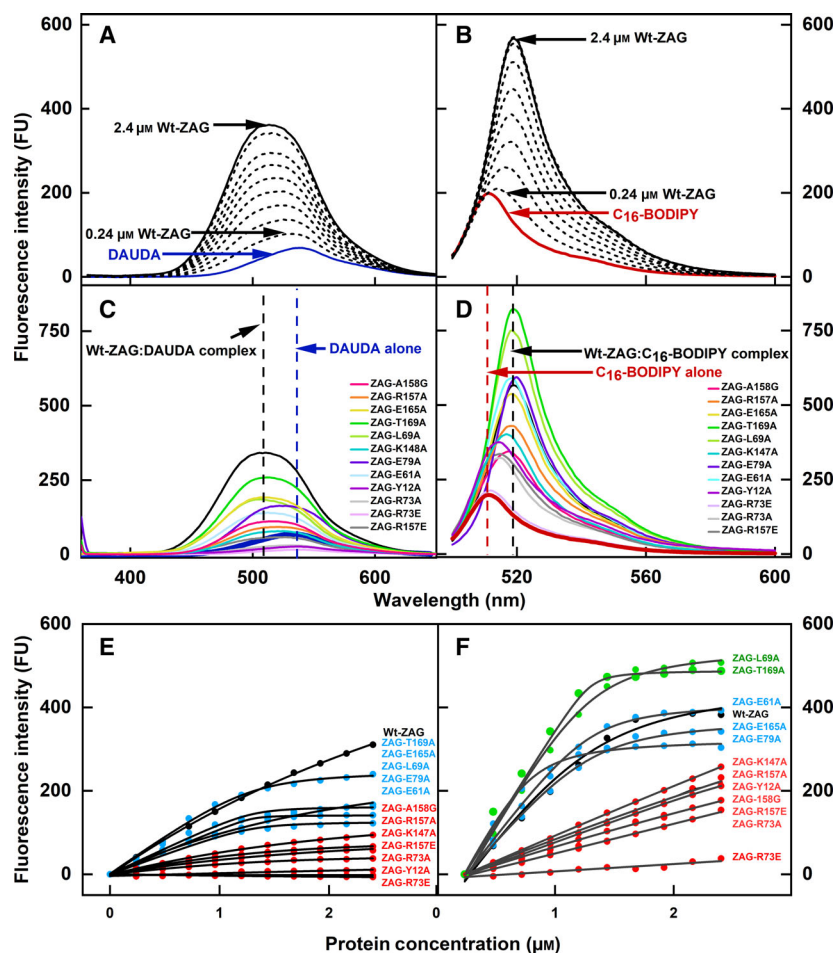


Fig. 7. Fluorescence emission spectra of DAUDA and C₁₆-BODIPY binding to Wt-ZAG and ZAG mutants. (A, B) Fluorescence emission spectra of 0.13 μM DAUDA and C₁₆-BODIPY when titrated with increasing Wt-ZAG concentrations in PBS buffer pH 7.4. (C, D) Fluorescence emission spectra for DAUDA or C₁₆-BODIPY, Wt-ZAG and 12 ZAG mutants. For clarity, the maximum emission wavelengths of DAUDA and C₁₆-BODIPY and their respective Wt-ZAG-ligand complexes are shown as vertical dashed lines. (E, F) Fluorescence titration curves of Wt-ZAG and 12 ZAG mutants binding with 0.13 μM DAUDA and 0.13 μM C₁₆-BODIPY. ZAG mutants were classed according to their effects on ligand binding; enhanced fluorescence emission intensity and tighter/similar binding affinity (smaller/similar K_d value; green), similar/slightly reduced binding fluorescence emission intensity and tighter/similar binding affinity (blue), or greatly reduced binding fluorescence emission intensity and similar binding affinity or greatly reduced binding affinity (red) in comparison to Wt-ZAG (black).

BODIPY fluorescence emission wavelength that indicated C₁₆-BODIPY binding was abolished, presumably due to electrostatic repulsion of the negatively charged C₁₆-BODIPY carboxylic acid group from the negatively charged glutamic acid residue (Fig. 7D, Fig. S5).

Next, a range of estimated K_d values was determined from the assays (Fig. 7F). For the T169A and E79A mutants, the K_d values of 0.006 and 0.002 μM respectively indicated tighter binding to C₁₆-BODIPY compared to Wt ZAG (0.16 μM) (Table 2). The K_d values for L69A, E61A and E165A were comparable to Wt ZAG, at 0.06, 0.04 and 0.08 μM, respectively (Fig. 7F and Table 2). The assays for the seven remaining mutants: K147A, R157A, Y12A, A158G, R157E, R73A and R73E (red in Fig. 7F) did not produce precise K_d values for C₁₆-BODIPY binding because saturation was not observed. These latter seven titrations indicated that the binding of C₁₆-BODIPY to each mutant was much reduced (looser binding being reflected in larger K_d values) in comparison with Wt ZAG and their values were outside the sensitivity measurement of the technique. In

approximate concordance with the K_d values, the C₁₆-BODIPY fluorescence emission intensities followed the order L69A = T169A > E61A = Wt-ZAG > E165A > E79A > K147A > R157A > Y12A > A158G > R157E > R73A > R73E (Fig. 7F).

Overall, the K147A, R157A, Y12A, A158G, R157E, R73A and R73E mutations abrogated C₁₆-BODIPY binding to ZAG. The alanine mutations of T169 and L69 caused enhanced C₁₆-BODIPY fluorescence emission intensities compared with Wt ZAG (green, Fig. 7F), presumably due to a different binding mode that produced an altered electronic state and increased fluorescence emission intensity.

As a benchmark and control, to determine whether C₁₆-BODIPY and DAUDA shared a common binding site in ZAG, Wt and mutant ZAG were likewise titrated with the fluorescent fatty acid DAUDA. The fluorescence emission intensity of DAUDA increases and exhibits a blue spectral shift in a hydrophobic environment. These properties have been observed for DAUDA binding to fatty acid binding proteins from nematodes [42–44], schistosomes [45], human

Table 2. Dissociation constants for the binding of Wt and mutant ZAG with C₁₆-BODIPY and DAUDA. DAUDA and C₁₆-BODIPY were individually titrated with ZAG and its mutant proteins. The resulting binding curves were fitted to a standard non-linear regression binding model as described in the Materials and Methods section to generate an estimated K_d value. R^2 values for each of the fitted binding curves are listed so that the fits can be evaluated.

Protein mutant ^a	C ₁₆ -BODIPY K_d (μM) ^b	C ₁₆ -BODIPY R^2 ^b	DAUDA K_d (μM) ^b	DAUDA R^2 ^b
L69A	0.06 ± 0.01	0.99665	0.02 ± 0.01	0.98057
T169A	0.006 ± 0.003	NA	0.07 ± 0.02	0.99566
E61A	0.04 ± 0.01	0.99838	0.03 ± 0.01	0.97007
Wt ZAG	0.16 ± 0.09	0.98503	3.48 ± 0.37	0.99964
E165A	0.08 ± 0.02	0.99674	0.65 ± 0.13	0.99876
E79A	0.002 ± 0.01	0.99694	0.10 ± 0.01	0.96602
K147A	–	–	1.15 ± 0.34	0.99766
R157A	–	–	0.39 ± 0.14	0.9992
R157E	–	–	0.37 ± 0.2	0.9975
A158G	–	–	1.26 ± 0.2	0.99894
R73A	–	–	–	–
R73E	–	–	–	–
Y12A	–	–	–	–

^aWt and mutant ZAG are listed in order of maximum emission intensities with C₁₆-BODIPY (Fig. 7).; ^bThe dash indicates that no reliable estimated K_d nor R^2 values were calculated. NA, not available.

intracellular fatty acid binding proteins [46] and human serum albumin [47]. When alone, 1.3 μM of DAUDA produces a maximum emission wavelength of 537 nm and a low fluorescence emission intensity (Fig. 7A). The addition of nine 0.24 μM aliquots of Wt ZAG to DAUDA caused a sequential increase in the fluorescence emission intensity and a blue shift in the maximum emission wavelength from 537 nm to 509 nm, to confirm that DAUDA bound to ZAG. The titration of DAUDA with ZAG did not reach saturation and yielded an estimated K_d value of $3.48 \pm 0.37 \mu\text{M}$ (Fig. 7E and Table 2), in close agreement with a previous independently determined ITC-generated K_d value of $1.3 \pm 0.4 \mu\text{M}$ for ZAG : DAUDA binding where signal saturation was achieved [32].

Titration of the 12 ZAG mutants with DAUDA were performed, and for each assay, changes in the DAUDA emission wavelength, K_d value and fluorescence emission intensity were again observed. Firstly, with DAUDA, the T169A, E165A, L69A and E61A mutants produced similar blue shifts in their maximum fluorescence emission wavelengths compared to Wt ZAG, from 537 nm to 510 nm, 509 nm, 507 nm and 512 nm, respectively, indicating that DAUDA bound to an unperturbed ZAG binding site (Fig. 7C; Figs S3 and S4). In comparison, E79A, A158G, R157A, K147A and R157E produced reduced blue shifts from 537 to 514 nm (E79A), 516 nm (A158G), 520 nm (R157A and K147A) and 525 nm (R157E). These reduced blue shifts were inferred to correspond to a more solvent exposed DAUDA binding site (Fig. 7C,

Figs S3–S5). Y12A, R73A and R73E produced no shift in the fluorescence emission intensity or wavelength upon addition to DAUDA, suggesting that these three mutations corresponded to misfolded protein or folded protein containing a disrupted DAUDA binding site (Fig. 7C, Fig. S5).

The K_d values for the T169A, L69A, E79A and E61A mutants displayed tighter DAUDA binding when compared with Wt-ZAG, being 0.07, 0.02, 0.1 and 0.03 μM , respectively (Fig. 7E and Table 2). The K_d values for E165A, A158G, R157A, K147A and R157E were 0.65, 1.26, 0.39, 1.15 and 0.39 μM , respectively, being similar to that of Wt-ZAG (Fig. 7E and Table 2). No K_d value was obtained for binding of R73A or R73E to DAUDA (Fig. 8E and Table 2); this agreed with our previous measurements [34]. No K_d value was obtained for binding of DAUDA to Y12A. The DAUDA fluorescence emission intensity was altered and followed the order Wt-ZAG > T169A > E165A > L69A > E79A > E61A > A158G > R157A > K147A > R157E > R73A > Y12A > R73E (Fig. 7E).

Overall, the R73A and R73E mutations abrogated DAUDA binding to ZAG while the A158G, R157A, K147A and R157E mutations showed DAUDA binding in a more solvent exposed ZAG binding groove.

Ligand screening

To further confirm the existence of separate but overlapping binding sites for DAUDA and C₁₆-BODIPY, fluorescence displacement assays were used to

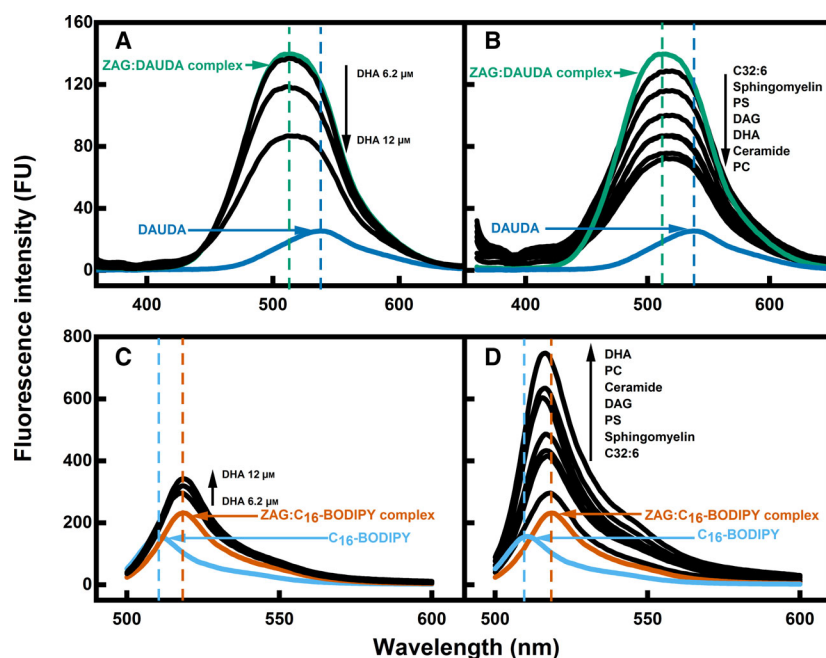


Fig. 8. Fluorescence displacement assays of DAUDA and C₁₆-BODIPY with seven lipid-based ligands. (A) DHA titrated in at 1.2 μM, 6 μM and 12 μM (black lines) to the ZAG-DAUDA complex (green solid line). (B) Summary of all seven lipids; DHA, PC, ceramide, DAG, PS, sphingomyelin and C32:6 each at 12 μM titrated to ZAG: DAUDA complex (green solid line). (C) DHA titrated in at 1.2 μM, 6 μM and 12 μM (black lines) to the ZAG-C₁₆-BODIPY complex (orange solid line). (D) Summary of all seven lipids; DHA, PC, ceramide, DAG, PS, sphingomyelin and C32:6 each at 12 μM titrated to the ZAG:C₁₆-BODIPY complex (orange solid line). In each panel, for clarity, the vertical dashed lines represent the fluorescence emission of DAUDA or C₁₆-BODIPY in buffer alone (blue), and the vertical dashed lines (green, orange) show the spectral shift upon the addition of Wt-ZAG.

determine the specificities of both binding sites for a range of lipids. Previous fluorescence displacement assays using DAUDA, revealed that ZAG showed preferential binding to long chain polyunsaturated fatty acids including DHA, eicosapentaenoic, linolenic, arachidonic and linoleic acids and also bound oleic acid but not cholesterol, deoxycholic acid or noradrenaline [32]. Indeed, the addition of excess DHA to a preformed ZAG-DAUDA complex reduced the DAUDA fluorescence emission intensity, this being explained by the competitive displacement of DAUDA from the ZAG groove (Fig. 8A), and as seen previously [38]. The interactions of ceramides with tear lipocalin were recently studied using fluorescence DAUDA displacement assays [48]. The addition of excess DHA to a preformed ZAG-C₁₆-BODIPY complex caused an increase in fluorescence emission intensity (Fig. 8C). This was surprising, given that others had shown that the addition of unlabelled oleic acid to preformed complexes of intestinal and liver fatty acid binding proteins complexed with C₁₆-BODIPY caused a reversal in the C₁₆-BODIPY fluorescence emission properties. This indicated competitive displacement of C₁₆-BODIPY by oleic acid from both fatty acid binding proteins [41]. Control experiments in the absence of ZAG, however, revealed the increase in fluorescence intensity was brought about by the interaction of C₁₆-BODIPY and DHA (Fig. S6B). Oxidative photo-induced electron transfer from the singlet excited state of the BODIPY fluorophore to an electron-poor chelator on the BODIPY probe causes an increase in

BODIPY fluorescence emission intensity [49]. Presumably, addition of DHA to C₁₆-BODIPY creates a complex that causes the C₁₆-BODIPY carboxylic acid (chelator) to become electron-poor and initiating the increase in fluorescence intensity. We conclude, therefore, that, unlike DAUDA, C₁₆-BODIPY was not displaced by DHA but DHA instead bound to the ZAG-C₁₆-BODIPY complex close to the bound C₁₆-BODIPY.

The addition of excess lipid to Wt ZAG-DAUDA complex resulted in the displacement of DAUDA from Wt ZAG for all lipids tested (Fig. 8B). These lipids included fatty acids (DHA and C32:6 fatty acid) and bulky lipids including phospholipids (phosphatidylcholine (PC) and phosphatidylserine (PS)), sphingolipids (ceramide and sphingomyelin) and diacylglyceride (DAG). In each case, a decrease in the DAUDA fluorescence intensity was observed upon addition of lipid to the preformed ZAG-DAUDA complex (Fig. 8B). All lipid ligands displaced DAUDA to different extents and in the order PC, ceramide, DAG = DHA, PS, sphingomyelin and C32:6 (Fig. 8B). The DAUDA binding site in ZAG is therefore able to accommodate very long chain fatty acids and bulky lipids, similar to the CD1 lipid presenting molecules. When these lipid displacement assays were repeated for the ZAG-C₁₆-BODIPY complexes, (Fig. 8D), unexpectedly the fluorescent intensities increased, as for DHA above. Control experiments in the absence of ZAG, revealed the increase in fluorescence intensity was brought about by the interaction of C₁₆-BODIPY with

individual lipids (Figs S6D,F,H and S7B,D,F). Again, we presume the addition of these fatty acids and bulky lipids to C₁₆-BODIPY creates complexes that cause the C₁₆-BODIPY carboxylic acid (chelator) to become electron poor and initiating the increase in fluorescence intensity [49]. C₁₆-BODIPY was therefore not displaced from ZAG by the range of tested fatty acids and bulky lipids presented here, but rather these lipids bound to the ZAG-C₁₆-BODIPY complex close to C₁₆-BODIPY. The ZAG groove can therefore accommodate more than one lipid simultaneously. Overall, these experiments confirmed that the C₁₆-BODIPY and DAUDA binding sites in ZAG were distinct from one another.

Liquid chromatography- mass spectrometry (LC-MS) detection of fatty acid binding to Wt ZAG

To directly confirm binding of the fatty acids to Wt ZAG, initial denaturing LC-MS experiments were used to directly verify the interactions of ZAG with DAUDA (molecular weight 434.6 g·mol⁻¹), C₁₆-BODIPY (molecular weight 474.44 g·mol⁻¹) and arachidonic acid (ARA, C20:4, molecular weight 304.5 g·mol⁻¹) (Fig. S8). ZAG eluted from the reversed phase column predominantly as a single peak (Fig. S8A) and produced a single peak with an *m/z* value of 32 274 upon deconvolution (Fig. S8B), almost identical to its theoretical mass of 32 273 Da. Single peaks with small shoulders and increased masses were observed for all three lipid-conjugated complexes. Upon deconvolution of each shoulder peak ZAG:lipid binding was clearly observed for DAUDA (Fig. S8B; 33 717) and C₁₆-BODIPY (Fig. S8G; 33 717) and corresponding to the addition of three molecules, and for ZAG:ARA (Fig. S8H; 32 581), one molecule.

Inductively coupled plasma-quadrupole mass spectrometry (ICP-QMS) quantification of zinc in Wt and mutant ZAG

Whether or not the ZAG mutants contain one molar equivalent of zinc in the same way as Wt ZAG was of interest. We had previously used ICP-MS to measure one tight zinc binding site in ZAG, which was attributed to the media in which the ZAG-containing *E. coli* construct was grown [36]. By computational scanning and molecular dynamic simulations, we predicted ZAG residues Asp90, His95 and Asp120 were most likely to form the tight zinc binding site in ZAG. This potential zinc binding site is located within the ZAG α 1- α 2 groove but far from the nine residues that were mutated during this study [36]. It was therefore

hypothesised that all mutant proteins would each contain one zinc ion. Surprisingly, our ICP-QMS measurements detected only tiny amounts of zinc in all proteins and not the expected one concentration equivalent (Fig. S9). Initially, ZAG and four mutant proteins (E61A, L69A, R73A and R157A) underwent buffer exchange using individual desalting columns before their use in ICP-QMS experiments. Following buffer exchange, three ZAG samples were spiked with a known amount of ZnCl₂ as a positive control. Approximately 0.8 concentration equivalents ([measured]/[theoretical]) of zinc were detected in these spiked samples (Fig. S9A) whereas only between 0.02 and 0.01 concentration equivalents ($[Zn]^{2+}/[ZAG]$) of zinc were detected in unspiked Wt ZAG and the four mutant proteins (Fig. S9B). To ensure that the desalting column had not removed any zinc bound within each protein, two samples of Wt ZAG underwent buffer exchange by dialysis before ICP-QMS measurements, thus replicating the sample preparation used in our 2014 ZAG-zinc measurements [36]. Here, these dialysed samples contained ~0.00003 concentration equivalents of zinc (Fig. S9C). We therefore concluded that Wt ZAG and the mutant proteins did not contain one tightly bound zinc ion.

Discussion

Our study has significantly expanded our understanding of the fatty acid binding properties of ZAG, in which we demonstrate a broader lipid specificity of ZAG than previously known. First, multiwavelength AUC experiments confirmed that the fluorescent fatty acids DAUDA and C₁₆-BODIPY bind to ZAG competitively at equimolar concentrations (Fig. 3). Next, a survey of 20 crystal structures for the structurally homologous CD1 fatty acid binding protein in complexes with fatty acids predicted that 20 residues in its α 1- α 2 groove may interact with their ligands. Of these, eleven had previously been examined by mutagenesis to verify their involvement [34], thus leaving nine more that were now examined in this study to complete this investigation (Fig. 4). These comprised seven potential fatty acid binding residues (Y12, E61, L69, R157, A158, E165 and T169) and two potential salt bridge forming residues (E79 and K147). All nine mutants were expressed, although two (R73A and Y12A) showed aberrant CD and AUC results, likely indicating perturbation of their structural folding (Fig. 6 and Fig. S2). Indeed, the ligand binding studies showed binding of C₁₆-BODIPY and DAUDA to both mutants was abrogated (Table 1). Mutation of K147, R157 and A158 abrogated C₁₆-BODIPY but not

DAUDA binding to ZAG (Table 1) and indicated that these are ZAG interacting residues that had not previously been identified to be involved in fatty acid binding. The remaining mutants all bound to both C₁₆-BODIPY and DAUDA. Increased C₁₆-BODIPY fluorescence emission intensities were witnessed upon binding of the probe to mutants L69 and T169 and indicated that C₁₆-BODIPY binds close to T169 and L69. Large, bulky signalling lipids were able to displace DAUDA from ZAG but not C₁₆-BODIPY. Overall, our data suggest overlapping C₁₆-BODIPY and DAUDA binding sites in ZAG and show that the functional binding region of the ZAG groove is larger than previously thought.

We independently checked our K_d estimates for DAUDA binding using reversed fluorescence titrations of 1.25, 2.5, 5 and 10 μM ZAG with increasing DAUDA concentrations (0–20 μM) in PBS. Saturated DAUDA signals were obtained with K_d values of 2.5, 1.9, 1.3 and 1.9 μM respectively that were within 10-fold agreement of our estimate of 3.48 μM and were therefore considered similar [50]. Using this same reversed fluorescence method, further titrations of DAUDA with A158G, E79A, E61A, R157E and R157A yielded saturated signals and K_d values of 3, 13, 5.6, 9 and 7 μM , respectively [50]. Our K_d value of 1.26 μM for A158G was within 10-fold of the reversed titration value. Our estimates of 0.1, 0.03, 0.39 and 0.39 μM for E79A, E61A and R157E and R157A respectively were over 10-fold smaller than those of the reversed titration values. Despite this, the mutant ZAG K_d values remain similar to those for Wt ZAG for each method used with the exception, in our case, of E79A and E61A, which show tighter binding than ZAG. These differences were explained by the lower R^2 value in our goodness of fit analyses and do not affect our overall conclusions.

Our recent ZAG-DAUDA crystal structure provides an explanation of the non-damaging nature of the A158G, R157A, K147A and R157E mutations to DAUDA binding and begins to reveal the residues involved in the C₁₆-BODIPY binding site and agrees with our denaturing LC-MS data [38]. The crystallographic ZAG: DAUDA unit cell contained six ZAG molecules (denoted as chains A–F) (PDB ID: 6RU2). Two different DAUDA binding co-ordinations were observed in the ZAG groove. The grooves of chains D, E and F each contained one bent DAUDA molecule. Chain B contained one extended DAUDA molecule buried in a wider groove and in a different position to those in chains D, E and F, plus two more DAUDA ligands that were bridged from chain B to the groove of the adjacent chain C. In agreement with

this observation, our denaturing LC-MS experiments identified three DAUDA molecules bound to ZAG (Fig. S8C,D). The grooves of chains A and C were empty of DAUDA. The different position of the extended DAUDA in chain B approached our predicted additional C₁₆-BODIPY binding site (Fig. 1). A158, R157 and K147 were predicted by molecular docking to have a high ZAG–ligand contact percentage (Fig. 4). However, in chains B, D, E and F of our crystal structure, neither A158, R157 nor K147 were involved in interactions with DAUDA [38], and hence DAUDA binding was unaffected by mutation of these residues in our ligand binding assays (Table 1). Our crystal structure thus explain why DAUDA binding was unaffected by mutation of A158, R157 and K147. Mutation of these residues did however abrogate C₁₆-BODIPY binding (Table 1). The extended DAUDA ligand in chain B measures 13.8 Å in length. While the bent DAUDA ligand in chain D measures 8.8 Å from its dansyl oxygen to its carboxylic oxygen. A distance of 14.1 Å was measured between the C α atoms of R157 and K147 in chain B. There are no crystal structure files for C₁₆-BODIPY making measurement of this ligand impossible. Assuming however, that it's extended and bent structures would be longer than 13.8 and 8.8 Å, respectively, it is feasible that an extended C₁₆-BODIPY be anchored by R157 and K147, interact with A158 and traverse the DAUDA binding site and thus account for the abrogation of C₁₆-BODIPY when these residues were mutated. In chain B, the distance between the guanidino groups of R73 and R157 is 20 Å while in chain D it is 12.6 Å. It is also therefore feasible that an extended or bent C₁₆-BODIPY could be anchored by R73 and R157 in a normal ZAG groove but not a widened one. We had initially hypothesised that K147 on the α 2 helix formed a salt bridge with E79 on the α 1 helix. However, distance measurements disproved this theory and showed that salt bridge formation was more likely between K147 and D83 on the α 1 helix. The K147 NZ–E79 OE2 charged group separations in *apo* ZAG (PDB ID: 6RU2 chains A and C), and the ZAG: DAUDA (PDB ID: 6RU2 chains B, D, E and F) and ZAG: PEG (PDB ID: 1T7V and 3ES6) complexes varied between 4.1 and 6.5 Å in eight measurements from three crystal structures, and these were larger than the upper distance limit of 4 Å indicative of salt bridge contacts [51]. However, the K147 NZ–D83 OD2 charged group separations in these three crystal structures varied between 2.9 and 3.4 Å, which is compatible with salt bridge formation. We concluded that A158 and R157 were crucial for C₁₆-BODIPY binding and that K147 was involved in salt bridge formation.

It is plausible that the K147-D83 salt bridge maintains the curvature of the ZAG groove that is required for C₁₆-BODIPY binding.

In turn, our ZAG-DAUDA crystal structure (PDB ID: 6R2U) also accounted for the binding of DAUDA and C₁₆-BODIPY to the five T169A, L69A, E165A, E79A and E61A ZAG mutants, despite the contacts predicted in Fig. 4 [38]. For the T169A mutation, the increased fluorescence emission intensity and affinity for C₁₆-BODIPY binding and increased affinity for DAUDA was clarified by inspection of ZAG-DAUDA chain B. Here, the carboxylic head group of DAUDA (Fig. 1) made two hydrogen bonds, one with the OH group of T169 and the other with its NH group of R73 [38]. The T169 mutation leaves the R73 NH group unaffected, meaning that its binding to DAUDA is unaffected. In chain B, the distance between the α -carbon atoms of R73 and T169 is 7.3 Å. An extended or bent C₁₆-BODIPY molecule could therefore encompass the R73-T169 residues in the widened ZAG groove. Presumably binding of C₁₆-BODIPY to the T169A mutant altered the local environment of this fluorescent probe, causing the C₁₆-BODIPY carboxylic acid (chelator) to become electron poor and increasing its fluorescence emission intensity [49]. The same appears true for the adjacent L69A mutation (Fig. 1), which also showed an increased fluorescence emission intensity for C₁₆-BODIPY. The increased intensities shown by C₁₆-BODIPY with these two mutants showed that this ligand binds close to T169 and L69 in the ZAG groove. Finally, the ligand-binding abilities of the E165A, E79A and E61A mutants were largely unaffected for both DAUDA and C₁₆-BODIPY. In the ZAG-DAUDA crystal structure, E79 is positioned on α -helix 1 and projects out of the groove, while E165 is located on α -helix 2 and projects into the groove. Neither residue forms direct contacts with DAUDA in the crystal structure [38], thus explaining why DAUDA binding was minimally affected. In like fashion, E61A showed minimal effects on DAUDA and C₁₆-BODIPY binding, revealing that neither DAUDA nor C₁₆-BODIPY bind near to E61 (Fig. 1).

Lastly, the crystal structures explained why the Y12A and R73A mutants disrupted the ZAG secondary and tertiary structures as revealed by CD and AUC data (Fig. 6 and Fig. S2). Unsurprisingly, both mutants also showed greatly reduced binding for DAUDA and C₁₆-BODIPY. Thus, residues Y12 and R73 play a structural and functional role in ZAG. Y12 is located towards the centre of the groove in β -strand 3 and close to R73 (Fig. 1). It forms two hydrogen bonds with a neighbouring residue, F101, on

β -strand 4. Mutation of F101 abrogated DAUDA ligand binding and resulted in the partial closure of the groove [34]. The Y12A mutation most likely disrupted the packing between these residues, resulting in the collapse of the groove. R73 was previously concluded to anchor fatty acid ligands and/or to keep the groove open [34]. R73 lies opposite R157 in the groove, which together form a region of positive charge that may mediate an open state of the groove through electrostatic repulsion. The R73A mutant disrupted the ZAG structure (Fig. 6 and Fig. S2), thus blocking DAUDA and C₁₆-BODIPY binding. Interestingly the R73E mutant had no effect on the ZAG structure, but abrogated DAUDA and C₁₆-BODIPY binding (Fig. 6 and Fig. S2). This would be in keeping with the negatively charged Glu residue repelling the negatively charged fatty acid to block the binding of the latter, while attracting the nearby positively charged R157 to maintain the structural integrity of the groove.

The ZAG : DAUDA crystal structure and our new results on the broader repertoire of lipids that can bind to ZAG are consistent with crystal structures of related protein-fatty acid complexes. In the fatty acid binding protein-7 crystal structure with oleic acid (PDB ID: 1FE3), the lipid interacted with F16, Y19, M20, L23, T36, P38, V40, T53 and R78 [52]. In the nuclear signalling protein PPAR γ (PDB ID: 2ZK6), C₈-BODIPY formed hydrophobic contacts with C285, R288, I326, L330 and I341 [53]. Two lipid binding sites within a single hydrophobic binding cavity are seen in the intracellular liver fatty acid binding protein [54] and the immune class I MHC CD1 protein family [55]. In CD1c (PDB ID: 6C09), D65 forms a salt bridge with K111 of its bound T cell antigen receptor [56].

We reinvestigated the tight zinc binding site in Wt ZAG in this study. No bound zinc ion had been observed in our recent ZAG : DAUDA crystal structure [38]. Here, mass spectrometry was not able to detect one concentration equivalent of zinc in Wt ZAG nor in its mutants, even though this had been revealed previously [36]. In 2014, the media used for ZAG protein expression was prepared from individual components. For the ZAG : DAUDA crystal structure work and for the work presented here, the media in which ZAG and the mutant proteins were expressed was premade. We therefore attribute the differences in the detection of zinc in ZAG between these different studies to the media used for protein expressions.

Other protein-lipid crystal structures extend our results. The bulky lipids tested here included phospholipids PC and PS, sphingolipids, sphingomyelin,

ceramide and DAG. These lipids displaced DAUDA from the ZAG groove (Fig. 8). These bulky lipids were unable to displace C₁₆-BODIPY from ZAG, indicating a distinct binding mode for C₁₆-BODIPY in contrast to DAUDA. In that context, the crystal structure of PC transfer protein in a 1 : 1 complex with PC (PDB ID: 1LN1) showed that the phosphorylcholine head group interacted with the hydrophilic side chains of Y72, Q157 and R78, and the methyl group of the lipid quaternary amine made contacts with V103, Y116 and Y175 and was inserted into an aromatic 'cage' formed from W101, Y114 and Y155 [57]. The structure of the steroidogenic acute regulatory protein-related lipid transfer domain of the ceramide transport protein, STARD11, in complex with C16, C18 and C24—ceramide (PDB ID: 2E3O, 2E3P, 2E3Q, 2E3R and 2E3S) showed that the amide/hydroxyl head group of ceramide formed hydrogen bonds with R442, E446, Q467, N504 and Y553. The residues F579, Y576, E575, A475, V472, V480, I523 and H469 formed hydrophobic interactions with ceramide [58]. In ZAG, residues E165, Y12 and R73 form a horizontal line across the ZAG groove. We speculate that the head groups of our bulky phospholipids are bound by these residues; thus, broadening ZAG's fatty acid binding site, with the aliphatic fatty acid chains stretching into the DAUDA binding site through hydrophobic interactions with Tyr, Trp, Phe and Ile.

Our findings in relation to broader lipid binding to ZAG can in the majority of cases be related to ZAG function. The fatty acids and bulky lipids that bind to ZAG (Fig. 8B) share functions in lipolysis, sperm motility, melanin production and tumour proliferation with ZAG. ZAG induces lipolysis either via interaction with β -adrenergic receptor or with AOC3 [11,15]. PC has recently been shown to induce lipolysis and apoptosis in mouse 3T3-L1 adipocytes albeit through TNF α and IL-1 β mediated pathways [59]. ZAG is expressed in human sperm [16] where it increases sperm motility in rams [17] and humans [16]. Levels of very long chain polyunsaturated fatty acids such as C32:6 show a positive correlation with sperm count and motility [60]. PS was recently shown to be exposed on the head region of viable and motile sperm and is required for fertilisation [61]. However, ZAG knock-out mice were fertile [6] suggesting that the ZAG-PS complex we observe here is not relevant to fertilisation. ZAG decreased melanin production in a B16F10 mouse melanoma cell line and caused the cells to form tumours with decreased tyrosinase activity [19]. Similarly, an artificial ceramide analogue inhibited melanin production and tyrosinase activity in a spontaneously immortalised melanocyte cell line, Mel-Ab [62]. The

introduction of ZAG to the human cervical tumour cell line SiHa reduced cell proliferation [20]. DHA inhibited the growth of SiHa cancer cells and promoted apoptosis [63]. In summary, the positive associations between ZAG and lipid functions suggest that the lipid to which ZAG binds could dictate ZAG function in the cell.

Materials and methods

Site-directed mutagenesis, protein expression and purification

The QuikChange™ II site directed mutagenesis kit (Agilent Technologies, Stockport, UK) was used for mutagenesis of the ZAG-containing pET23a-AZGP1 vector clone following the manufacturer's protocol. PCR was used with template pET23a-AZGP1 DNA and mutagenic primers to amplify mutated ZAG DNA. Complementary mutagenic primers containing the desired point mutation were designed using the QuikChangecode>™ primer design online tool (Agilent Technologies) with the exceptions of ZAG-T169A, ZAG-Y12A and ZAG-R73E, which were designed manually. All primers were synthesised and purified to HPLC grade by Sigma Aldrich, Poole, UK. Following PCR, the enzyme *DpnI* was used to digest the parental template DNA and the mutated DNA was transformed into XL1-Blue super competent cells. The success of the mutagenesis reactions was verified by DNA sequencing (Source Bioscience, Nottingham, UK) using the T7-forward and T7-reverse primers. Sequencing data were analysed using Chromas Lite software. Purified mutated ZAG DNA was transformed into BL21 DE3 pLysE *Escherichia coli* cells for protein expression. ZAG and its mutant proteins formed inclusion bodies when expressed with 0.8 mM IPTG in *E. coli*. The inclusion bodies were denatured in 6 M guanidine HCl and refolded using the hyper dilution method described previously [36]. Refolded wild-type (Wt) ZAG and mutant proteins were purified using a GE Superdex 75 size-exclusion chromatography column equilibrated with phosphate buffered saline (PBS; 2.7 mM KCl, 1.5 mM KH₂PO₄, 137 mM NaCl, 8 mM Na₂HPO₄) at a flow rate of 2 mL·min⁻¹ at 22 °C using an Akta Pure and Unicorn software (Cytiva, Amersham, UK). Protein containing fractions were collected and concentrated. Protein concentration was determined by the absorbance A at 280 nm using an Implen NanoPhotometer NP80 (Munich, Germany) and the Beer-Lambert law ($A = \epsilon lc$) where l is the path thickness. The theoretical extinction coefficient was taken as $\epsilon_{280 \text{ nm}} = 71\,071 \text{ M}^{-1}\cdot\text{cm}^{-1}$ for ZAG and the ZAG-mutants with the exception of ZAG-Y12A for which $\epsilon_{280 \text{ nm}}$ was 69 580 M⁻¹·cm⁻¹. Theoretical molar extinction coefficients were calculated using the ExPASy ProtParam tool [64]. The purities of Wt-ZAG and the ZAG-mutants were further verified using a NuPAGE 4–12% gradient Bis-

tris SDS polyacrylamide gel, staining with Coomassie Blue (Life Technologies, Paisley, UK).....

AUC data collection

AUC sedimentation velocity experiments were performed using a Proteome XL-I instrument and a multi-wavelength Optima AUC instrument (Beckman Coulter, High Wycombe, UK), equipped with An50Ti rotors and using velocity cells with two-sector aluminium centrepieces, at rotor speeds of 50 000 rpm at 20 °C. To determine the oligomeric state of Wt and mutant ZAG proteins, sedimentation velocity experiments were performed on the Proteome XL-I at concentrations between 0.26 and 1.04 mg·mL⁻¹ in phosphate buffered saline (PBS; 2.7 mM KCl, 1.5 mM KH₂PO₄, 137 mM NaCl, 8 mM Na₂HPO₄). For sedimentation velocity experiments of the ZAG-fatty acid complexes, the dansyl-labelled C₁₁ fatty acid DAUDA (11-[5-(dimethylamino)-1-naphthalenesulfonylamino] undecanoic acid), and the boron dipyrromethane C₁₆ fatty acid C₁₆-BODIPY (4,4-difluoro-5,7-dimethyl-4-bora-3a,4a-diaza-s-indacene-3-hexadecanoic acid) were used. These were stored as stock solutions of ~2 mg·mL⁻¹ in ethanol and 1.5 mg·mL⁻¹ in DMSO, respectively, at -20 °C in the dark.

The multi-wavelength Optima AUC was set up to detect the sedimentation of ZAG protein at 280 nm, DAUDA at 335 nm and C₁₆-BODIPY at 515 nm. Control AUC experiments without ZAG showed that the free fluorescent fatty acids themselves did not sediment. The ZAG-fatty acid complexes were prepared in PBS at a constant ZAG concentration of 0.36 mg·mL⁻¹ (11 µM) with different concentrations of DAUDA and/or C₁₆-BODIPY. Ethanol and DMSO were added to PBS in the buffer blank cells to match the amounts of DAUDA and/or C₁₆-BODIPY in the sample cells. The densities and viscosities of these buffers were measured using an Anton Paar DMA 5000 density metre at 20 °C. SEDFIT software (version 15.1) [65,66] was used to analyse each of the absorbance data sets collected at 280 nm (ZAG and ZAG mutants), 335 nm (DAUDA) and 515 nm (C₁₆-BODIPY). The Lamm equation was fitted to every third/fifth boundary scan of a total of 136 scans in order to obtain the size distribution analyses *c*(*s*), which provided *s*_{20,w} and mass values. The *c*(*s*) analyses were based on a fixed resolution of 200, minimum and maximum sedimentation (*s*_{min} and *s*_{max}) of 0.5 S and 15 S, respectively, and a frictional ratio of 1.2. The distribution was optimised by floating the meniscus, bottom of the cell and baseline until visual appearance and root mean square deviations were satisfactory (< 0.02). The percentage of any oligomers was obtained from the *c*(*s*) integration function.

Molecular docking

Crystallographic CD1 ligands were extracted from existing CD1a-d crystal structures (Table S1). All ligand data files

were converted to AutoDock Vina-compatible PDBQT format using OpenBabel software [67]. Molecular docking was performed using AutoDock Vina using default parameters unless specified otherwise [68]. The search space of the structure of ZAG (PDB ID: 1T7Z) was set at center_x = -3.054, center_y = 78.555 and center_z = -26.763, with dimensions size_x = 98, size_y = 78.555 and size_z = 114. Ligands docked in the proximity of the ZAG groove were then analysed using LIGPLOT software to identify interacting residues [69]. All residues which interacted with > 25% of docked ligands were designated as being potentially involved in lipid binding *ex silico*.

Multiple sequence alignment of ZAG sequences

The canonical native sequence of human ZAG (UniProt: P25311) was aligned together with ZAG sequences from other species, using the T-Coffee webserver with default parameters <http://tcoffee.crg.cat/apps/tcoffee/do:regular> [70]. Sequences were sourced from: Western Lowland Gorilla (UniProt: G3QHX6), Sumatran Oranutan (UniProt: H2PLK8), Green Monkey (UniProt: A0A0D9RZ11), Olive Baboon (UniProt: A0A096N8U6), Rhesus Macaque (UniProt: F6YWS9), Northern White-Cheeked Gibbon (UniProt: G7P0C0), White-Tufted-Ear Marmoset (UniProt: F6W5A5), Bovine (UniProt: Q3ZCH5), Mouse (UniProt: Q64726) and Rat (UniProt: Q63678). The positions of the putative lipid-interacting residues of the ZAG groove identified from molecular docking analyses were evaluated from the resultant alignment to assess conservation across species.

CD spectroscopy

Near and far UV CD spectra of Wt-ZAG and the ZAG-mutants were recorded on a JASCO UK Ltd (Essex, UK) J-810 spectropolarimeter (JASCO, UK Ltd) using quartz cells with a path length of 0.5 cm. All measurements were made at 24 °C with protein concentrations between 0.1 and 0.5 mg·mL⁻¹ as calculated by the absorbance A_{280nm} prior to data acquisition in 50 mM Na₂HPO₄, pH 7.4. Spectra were corrected for concentration, cell pathlength and buffer contribution.

Fluorescence spectroscopy

Fluorescence measurements were recorded at 22 °C with a Perkin Elmer (Llantrisant, UK) LS50B Luminescence Spectrometer using 2 mL samples in a 4 mL capacity quartz cuvette in PBS. C₁₆-BODIPY and DAUDA (Life Technologies) were stored as stock solutions of 1.5 mg·mL⁻¹ in DMSO and 2 mg·mL⁻¹ in ethanol, respectively, at -20 °C in the dark. They were freshly diluted to 0.15 mg·mL⁻¹ (316 µM) and 0.2 mg·mL⁻¹ (460 µM) in ethanol before use in experiments. C₁₆-BODIPY was further diluted to 1.3 µM

in PBS and titrated with increasing concentrations of Wt-ZAG and ZAG-mutants in protein aliquots of 22–185 μL in separate experiments until final protein concentrations of 2.4 μM were reached in final volumes that ranged between 2.23 and 3.86 mL. C_{16} -BODIPY was excited at 488 nm and fluorescence emission data were collected between 500 and 600 nm. Similarly, 1.3 μM DAUDA was titrated with increasing concentrations of Wt-ZAG and ZAG-mutants in protein aliquots of 22–190 μL in separate experiments until final protein concentrations of 2.4 μM were reached in final volumes that ranged between 2.23 and 3.86 mL. DAUDA was excited at 345 nm and fluorescence emission data were collected between 350 and 650 nm. All fluorescence spectra were corrected for the effects of dilution by multiplying by a dilution factor. Raman scattering was accounted for by subtracting the buffer-only spectrum from individual spectra. The resulting binding curves were fitted to a single non-competitive binding model to calculate the dissociation constant (K_d) for DAUDA and C_{16} -BODIPY binding. The binding model was derived from consideration of the standard equilibrium binding of a protein (P) and ligand (L) defined as $\text{P} + \text{L} \leftrightarrow \text{PL}$ with $K_d = [\text{P}][\text{L}]/[\text{PL}]$. This is described as follows: $F(\text{observed}) = F1 + \frac{(F2-F1)(x+nC0+kd)}{2nC0} \left[1 - \sqrt{\frac{1-4nC0}{(x+nC0+kd)^2}} \right]$ where F1 is the initial fluorescence intensity (without ligand), F2 is the fluorescence intensity for the fully bound state, x is the total protein concentration, $C0$ is the total ligand concentration, and n is the number of binding sites per protein that are assumed to be independent and non-interacting. The assumption of a 1 : 1 stoichiometry follows earlier ITC experiments of the binding of DAUDA to ZAG that indicated this [32]. Thus n was fixed at 1 for fitting the DAUDA titrations, and also for the C_{16} -BODIPY titrations. For fluorescence displacement studies, the following lipids were stored at -20°C in the dark and prepared as 5 $\text{mg}\cdot\text{mL}^{-1}$ stock solutions; docosahexaenoic acid (DHA) in ethanol, ceramide derived from bovine spinal cord in chloroform/methanol (3 : 1), N-Acyl-D-sphingosine-1-phosphocholine (sphingomyelin) from chicken egg yolk in chloroform/methanol (3 : 1), and L- α -PC from chicken egg yolk in chloroform/methanol (3 : 1) (Sigma Aldrich, Poole). 1-2-Dioleoyl-sn-glycerol (DAG 18 : 1) in chloroform, and L- α -PS from porcine brain in chloroform (Avanti Polar Lipids, Birmingham, AL, USA). 14Z,17Z,20Z,23Z,26Z,29Z-dotriacontahexaenoic acid (C32:6 fatty acid) was stored as a 1 $\text{mg}\cdot\text{mL}^{-1}$ stock solution in methylene chloride (Avanti Polar Lipids). All lipids were freshly diluted into ethanol prior to use in fluorescence displacement assays. Three additions of each lipid (1.2, 6 and 12 μM) were added to pre-formed ZAG:DAUDA or ZAG: C_{16} -BODIPY complexes in a molar ratio of 1.2 μM : 1.3 μM and the fluorescence emission spectra were recorded. Control experiments involving titration of lipids with both fluorescent fatty acid probes in the absence of ZAG were also performed (Figs S5 and S6).

Liquid chromatography- mass spectrometry

Wt ZAG and ZAG: fatty acid samples were analysed on the Agilent 6510 QTOF LC-MS system in the UCL Chemistry Mass Spectrometry Facility. Ten microlitres of each sample ($\sim 0.2 \text{ mg}\cdot\text{mL}^{-1}$ of protein) were injected onto a PLRP-S, 1000A, 8 μm , $150 \times 2.1 \text{ mm}^2$ column, which was maintained at 60°C . Sample separation was achieved using mobile phase A (water with 0.1% formic acid) and B (acetonitrile, with 0.1% formic acid) using a gradient elution at the flow rate $0.3 \text{ mL}\cdot\text{min}^{-1}$. The column effluent was continuously electrosprayed into the capillary electrospray ionisation (ESI) source of the Agilent 6510 QTOF mass spectrometer. ESI mass spectra were acquired in positive ESI mode at the m/z range 1000–3200 in profile mode. The raw data was converted to zero charge mass spectra using maximum entropy deconvolution algorithm within the MassHunter software version B.07.00.

Inductively coupled plasma-quadropole mass spectrometry

To quantify the number of zinc ions associated with ZAG and its mutant proteins, one Wt ZAG and four mutant ZAG protein preparations (E61A, L69A, R73A and R157E) underwent ICP-QMS measurements. All proteins were purified in PBS as described above and stored at -20°C before use in ICP-QMS experiments. Protein samples were thawed on ice and their concentrations determined using their $A_{280 \text{ nm}}$ values, theoretical molecular weights and an extinction coefficient of $71\,071 \text{ M}^{-1}\cdot\text{cm}^{-1}$. For the first set of measurements, samples were prepared in triplicate by undergoing buffer exchange into 10 mM Hepes, pH 7.2 using individual Zeba Spin desalting columns, 7 kDa MWCO (Thermo Fisher Scientific, Waltham, MA, USA) and following the manufacturers guidelines. As a positive control, three ZAG samples that were eluted from three individual ion removal columns and were spiked with $654 \mu\text{g}\cdot\text{L}^{-1}$ of zinc chloride (Sigma Aldrich, Dorset, UK); 60 μL samples were diluted by a factor of $\times 50$ using 0.3 M HNO_3 (67–69% w/w; Thermo Fisher Scientific) and purified water with a resistivity $\geq 18.2 \text{ M}\Omega \text{ cm}$ from an Milli Q system (Millipore Sigma, Burlington, MA, USA) to a final volume of 3 mL in 15 mL acid cleaned trace metal grade HDPE centrifuge tubes (VWR, Dorset, UK). In a second set of measurements, two ZAG samples underwent dialysis into 10 mM Hepes, pH 7.2; 700 μL of these samples were diluted by a factor of $\times 3.2$ to a final volume of 2.24 mL as above. A part of the dilution involved doping all samples with the internal standard Ga using a $100 \text{ mg}\cdot\text{L}^{-1}$ standard solution (Teledyne Leeman Labs, Mason, OH, USA) to obtain sample concentrations of $50 \mu\text{g Ga}\cdot\text{L}^{-1}$. Zinc calibration standards were made volumetrically using a $100 \text{ mg}\cdot\text{L}^{-1}$ TraceCert multi-element standard (Sigma Aldrich, Dorset, UK), a 0.3 M HNO_3 stock solution made

from Optima grade concentrated HNO₃ and purified water. Zinc concentrations of the calibrants were between 0.1 and 1000 µg·L⁻¹ and all calibration solutions, like the samples, were doped with a 100 mg·L⁻¹ Ga standard solution (Teledyne Leeman Labs) to obtain a concentration of 50 µg Ga·L⁻¹, which was used for internal normalisation of sample measurements.

All measurements were conducted on a Perkin Elmer NexION 350D ICP-QMS under Dynamic Reaction Cell mode at the London Metallomics Facility, King's College London. The introduction system to the instrument was a Cetac ASX-100 autosampler coupled to a SeaSpray glass nebulizer fitted to a quartz cyclonic spray chamber. Argon plasma flow and nebulizer gas flow rates were 18 and 0.96 L·min⁻¹, respectively. Quality control of ICP-QMS measurements was ensured through repeat measurements of acid blanks, a calibrant and a certified reference material CRM-TMDW-100 (High Purity Standards, North Charleston, SC, USA). Zinc measurements were normalised to the internal Ga standard to account for instrument drift and matrix effects, and measurements were subsequently blank corrected by removing the average analyte intensity of repeat blank measurements. The corrected zinc intensity was converted to concentration values (µg L⁻¹) using the linear equation generated by the calibration curve of the standards. Sample zinc concentration values were further corrected by subtraction of a buffer only value. Protein concentration measurements were converted to µg L⁻¹ to enable the calculation of zinc:protein ratios.

Acknowledgements

We thank Dr Gemma Harris and Dr David J. Scott (Research Complex at Harwell) for access to a Beckman-Coulter Optima AUC instrument and the Capital Equipment Fund of University College London for the purchase of our own Optima AUC instrument. We thank Dr Theodora Stewart, Dr Alex Griffiths and Dr Maral Amrahi (London Metallomics Facility, King's College London) for help with the ICP-QMS measurements. HZ, AL, SJP and LCM were supported by Biotechnology and Biological Sciences Research Council BBSRC LIDO PhD studentship awards [grant number BB/M009513/1]. Financial support to LCM was provided from a purchasing and licencing agreement with the biotechnology company AdipoGen International and was used to conduct this research.

Conflict of interest

LCM holds a purchasing and licencing agreement with the biotechnology company AdipoGen International.

Author contributions

HZ, LCM and SJP designed the study and wrote the paper. JG performed the AUC data collection. AML predicted ligand interacting residues of ZAG. HZ performed site directed mutagenesis, protein expression, purification and fluorescence binding assays. SMK collected CD data. KK collected LC-MS data. All authors analysed the results and approved the final version of the manuscript.

Peer review

The peer review history for this article is available at <https://publons.com/publon/10.1111/febs.16293>.

Data availability statement

The data that supports the findings of this study are available in the supporting information of this article.

References

- 1 Hale LP, Price DT, Sanchez LM, Demark-Wahnefried W & Madden JF (2001) Zinc alpha-2-glycoprotein is expressed by malignant prostatic epithelium and may serve as a potential serum marker for prostate cancer. *Clin Cancer Res* **7**, 846–853.
- 2 Tada T, Ohkubo I, Niwa M, Sasaki M, Tateyama H & Eimoto T (1991) Immunohistochemical localization of Zn-alpha 2-glycoprotein in normal human tissues. *J Histochem Cytochem* **39**, 1221–1226.
- 3 Burgi W & Schmid K (1961) Preparation and properties of Zn-alpha 2-glycoprotein of normal human plasma. *J Biol Chem* **236**, 1066–1074.
- 4 Poortmans JR & Schmid K (1968) The level of Zn-alpha 2-glycoprotein in normal human body fluids and kidney extract. *J Lab Clin Med* **71**, 807–811.
- 5 Hirai K, Hussey HJ, Barber MD, Price SA & Tisdale MJ (1998) Biological evaluation of a lipid-mobilizing factor isolated from the urine of cancer patients. *Cancer Res* **58**, 2359–2365.
- 6 Rolli V, Radosavljevic M, Astier V, Macquin C, Castan-Laurell I, Visentin V, Guigne C, Carpenne C, Valet P, Gilfillan S *et al.* (2007) Lipolysis is altered in MHC class I zinc-alpha(2)-glycoprotein deficient mice. *FEBS Lett* **581**, 394–400.
- 7 Russell ST & Tisdale MJ (2010) Antidiabetic properties of zinc-alpha2-glycoprotein in ob/ob mice. *Endocrinology* **151**, 948–957.
- 8 Mracek T, Gao D, Tzanavari T, Bao Y, Xiao X, Stocker C, Trayhurn P & Bing C (2010) Downregulation of zinc-alpha2-glycoprotein in adipose tissue and liver of obese

- ob/ob mice and by tumour necrosis factor- α in adipocytes. *J Endocrinol* **204**, 165–172.
- 9 Selva DM, Lecube A, Hernandez C, Baena JA, Fort JM & Simo R (2009) Lower zinc- α 2-glycoprotein production by adipose tissue and liver in obese patients unrelated to insulin resistance. *J Clin Endocrinol Metab* **94**, 4499–4507.
 - 10 Bing C, Bao Y, Jenkins J, Sanders P, Manieri M, Cinti S, Tisdale MJ & Trayhurn P (2004) Zinc- α 2-glycoprotein, a lipid mobilizing factor, is expressed in adipocytes and is up-regulated in mice with cancer cachexia. *Proc Natl Acad Sci USA* **101**, 2500–2505.
 - 11 Russell ST, Hirai K & Tisdale MJ (2002) Role of beta3-adrenergic receptors in the action of a tumour lipid mobilizing factor. *Br J Cancer* **86**, 424–428.
 - 12 Wargent ET, O'Dowd JF, Zaibi MS, Gao D, Bing C, Trayhurn P, Cawthorne MA, Arch JR & Stocker CJ (2013) Contrasts between the effects of zinc- α 2-glycoprotein, a putative beta3/2-adrenoceptor agonist and the beta3/2-adrenoceptor agonist BRL35135 in C57Bl/6 (ob/ob) mice. *J Endocrinol* **216**, 157–168.
 - 13 Elattar S, Dimri M & Satyanarayana A (2018) The tumor secretory factor ZAG promotes white adipose tissue browning and energy wasting. *FASEB J* **32**, 4727–4743.
 - 14 Xiao XH, Qi XY, Wang YD, Ran L, Yang J, Zhang HL, Xu CX, Wen GB & Liu JH (2018) Zinc α 2 glycoprotein promotes browning in adipocytes. *Biochem Biophys Res Commun* **496**, 287–293.
 - 15 Romauch M (2020) Zinc- α 2-glycoprotein as an inhibitor of amine oxidase copper-containing 3. *Open Biol* **10**, 190035.
 - 16 Qu F, Ying X, Guo W, Guo Q, Chen G, Liu Y & Ding Z (2007) The role of Zn- α 2 glycoprotein in sperm motility is mediated by changes in cyclic AMP. *Reproduction* **134**, 569–576.
 - 17 Soleilhavoup C, Tsikis G, Labas V, Harichaux G, Kohnke PL, Dacheux JL, Guerin Y, Gatti JL, de Graaf SP & Druart X (2014) Ram seminal plasma proteome and its impact on liquid preservation of spermatozoa. *J Proteomics* **109**, 245–260.
 - 18 Takagaki M, Honke K, Tsukamoto T, Higashiyama S, Taniguchi N, Makita A & Ohkubo I (1994) Zn- α 2-glycoprotein is a novel adhesive protein. *Biochem Biophys Res Commun* **201**, 1339–1347.
 - 19 Hale LP (2002) Zinc α -2-glycoprotein regulates melanin production by normal and malignant melanocytes. *J Invest Dermatol* **119**, 464–470.
 - 20 He N, Brysk H, Tying SK, Ohkubo I & Brysk MM (2001) Zinc- α (2)-glycoprotein hinders cell proliferation and reduces cdc2 expression. *J Cell Biochem Suppl* **36**, 162–169.
 - 21 Boersema PJ, Geiger T, Wisniewski JR & Mann M (2013) Quantification of the N-glycosylated secretome by super-SILAC during breast cancer progression and in human blood samples. *Mol Cell Proteomics* **12**, 158–171.
 - 22 Whelan SA, He J, Lu M, Souda P, Saxton RE, Faull KF, Whitelegge JP & Chang HR (2012) Mass spectrometry (LC-MS/MS) identified proteomic biosignatures of breast cancer in proximal fluid. *J Proteome Res* **11**, 5034–5045.
 - 23 Zhu H, Liu M, Zhang N, Pan H, Lin G, Li N, Wang L, Yang H, Yan K & Gong F (2018) Circulating and adipose tissue mRNA levels of Zinc- α 2-glycoprotein, leptin, high-molecular-weight adiponectin, and tumor necrosis factor- α in colorectal cancer patients with or without obesity. *Front Endocrinol* **9**, 190.
 - 24 Pelletier CC, Koppe L, Alix PM, Kalbacher E, Croze ML, Hadj-Aissa A, Fouque D, Guebre-Egziabher F & Soulage CO (2014) The relationship between renal function and plasma concentration of the cachectic factor zinc- α 2-glycoprotein (ZAG) in adult patients with chronic kidney disease. *PLoS One* **9**, e103475.
 - 25 Tedeschi S, Pilotti E, Parenti E, Vicini V, Coghi P, Montanari A, Regolisti G, Fiaccadori E & Cabassi A (2012) Serum adipokine zinc α 2-glycoprotein and lipolysis in cachectic and noncachectic heart failure patients: relationship with neurohormonal and inflammatory biomarkers. *Metabolism* **61**, 37–42.
 - 26 Xu L, Yu W, Niu M, Zheng C, Qu B, Li Y, Wang J, Huang P, Wang O & Gong F (2017) Serum ZAG levels were associated with eGFR mild decrease in T2DM patients with diabetic nephropathy. *Int J Endocrinol* **2017**, 5372625.
 - 27 Zhu HJ, Wang XQ, Pan H, Gong FY, Zhang DX, Li NS, Wang LJ & Yang HB (2014) Serum levels of the adipokine Zinc- α 2-glycoprotein are decreased in patients with hypertension. *ISRN Endocrinol* **2014**, 374090.
 - 28 Sanchez LM, Chirino AJ & Bjorkman P (1999) Crystal structure of human ZAG, a fat-depleting factor related to MHC molecules. *Science* **283**, 1914–1919.
 - 29 Berg JM, Tymoczko JL & Stryer L (2002) Major-Histocompatibility-Complex Proteins Present Peptide Antigens on Cell Surfaces for Recognition by T-Cell Receptors in Biochemistry. W. H. Freeman, New York.
 - 30 Sanchez LM, Lopez-Otin C & Bjorkman PJ (1997) Biochemical characterization and crystallization of human Zn- α 2-glycoprotein, a soluble class I major histocompatibility complex homolog. *Proc Natl Acad Sci USA* **94**, 4626–4630.
 - 31 Storch J & McDermott L (2009) Structural and functional analysis of fatty acid-binding proteins. *J Lipid Res* **50**(Suppl), S126–S131.
 - 32 Kennedy MW, Heikema AP, Cooper A, Bjorkman PJ & Sanchez LM (2001) Hydrophobic ligand binding by Zn- α 2-glycoprotein, a soluble fat-depleting factor related to major histocompatibility complex proteins. *J Biol Chem* **276**, 35008–35013.

- 33 Delker SL, West AP Jr, McDermott L, Kennedy MW & Bjorkman PJ (2004) Crystallographic studies of ligand binding by Zn-alpha2-glycoprotein. *J Struct Biol* **148**, 205–213.
- 34 McDermott LC, Freel JA, West AP, Bjorkman PJ & Kennedy MW (2006) Zn-alpha2-glycoprotein, an MHC class I-related glycoprotein regulator of adipose tissues: modification or abrogation of ligand binding by site-directed mutagenesis. *Biochemistry* **45**, 2035–2041.
- 35 Zahid H, Miah L, Lau AM, Brochard L, Hati D, Bui TT, Drake AF, Gor J, Perkins SJ & McDermott LC (2016) Zinc-induced oligomerization of zinc alpha2 glycoprotein reveals multiple fatty acid-binding sites. *Biochem J* **473**, 43–54.
- 36 Kumar AA, Hati D, Thaker TM, Miah L, Cunningham P, Domene C, Bui TT, Drake AF & McDermott LC (2013) Strong and weak zinc binding sites in human zinc-alpha2-glycoprotein. *FEBS Lett* **587**, 3949–3954.
- 37 Garcia-Alles LF, Giacometti G, Versluis C, Maveyraud L, de Paeppe D, Guiard J, Tranier S, Gilleron M, Prandi J, Hanau D *et al.* (2011) Crystal structure of human CD1e reveals a groove suited for lipid-exchange processes. *Proc Natl Acad Sci USA* **108**, 13230–13235.
- 38 Lau AM, Zahid H, Gor J, Perkins SJ, Coker AR & McDermott LC (2019) Crystal structure of zinc-alpha2-glycoprotein in complex with a fatty acid reveals multiple different modes of protein-lipid binding. *Biochem J* **476**, 2815–2834.
- 39 Kelly SM & Price NC (2000) The use of circular dichroism in the investigation of protein structure and function. *Curr Protein Pept Sci* **1**, 349–384.
- 40 Scott DJSP (2005) A brief introduction to the analytical ultracentrifugation of proteins for beginners. In *Modern Analytical Ultracentrifugation: Techniques and Methods* (Scott DJ, Harding SE & Rowe AJ, eds), pp. 1–25. Royal Society of Chemistry, London, UK.
- 41 Thumser AE & Storch J (2007) Characterization of a BODIPY-labeled fluorescent fatty acid analogue, binding to fatty acid-binding proteins, intracellular localization, and metabolism. *Mol Cell Biochem* **299**, 67–73.
- 42 McDermott L, Moore J, Brass A, Price NC, Kelly SM, Cooper A & Kennedy MW (2001) Mutagenic and chemical modification of the ABA-1 allergen of the nematode *Ascaris*: consequences for structure and lipid binding properties. *Biochemistry* **40**, 9918–9926.
- 43 Moore J, McDermott L, Price NC, Kelly SM, Cooper A & Kennedy MW (1999) Sequence-divergent units of the ABA-1 polyprotein array of the nematode *Ascaris suum* have similar fatty-acid- and retinol-binding properties but different binding-site environments. *Biochem J* **340**(Pt 1), 337–343.
- 44 Zhan B, Arumugam S, Kennedy MW, Tricoche N, Lian LY, Asojo OA, Bennuru S, Bottazzi ME, Hotez PJ, Lustigman S *et al.* (2018) Ligand binding properties of two *Brugia malayi* fatty acid and retinol (FAR) binding proteins and their vaccine efficacies against challenge infection in gerbils. *PLoS Negl Trop Dis* **12**, e0006772.
- 45 Kennedy MW, Scott JC, Lo S, Beauchamp J & McManus DP (2000) Sj-FABPc fatty-acid-binding protein of the human blood fluke *Schistosoma japonicum*: structural and functional characterization and unusual solvent exposure of a portal-proximal tryptophan residue. *Biochem J* **349**, 377–384.
- 46 Patil R, Laguerre A, Wielens J, Headey SJ, Williams ML, Hughes ML, Mohanty B, Porter CJ & Scanlon MJ (2014) Characterization of two distinct modes of drug binding to human intestinal fatty acid binding protein. *ACS Chem Biol* **9**, 2526–2534.
- 47 Wilton DC (1990) The fatty acid analogue 11-(dansylamino)undecanoic acid is a fluorescent probe for the bilirubin-binding sites of albumin and not for the high-affinity fatty acid-binding sites. *Biochem J* **270**, 163–166.
- 48 Glasgow BJ & Abduragimov AR (2018) Interaction of ceramides and tear lipocalin. *Biochim Biophys Acta Mol Cell Biol Lipids* **1863**, 399–408.
- 49 Boens N, Leen V & Dehaen W (2012) Fluorescent indicators based on BODIPY. *Chem Soc Rev* **41**, 1130–1172.
- 50 Pan KS (2020) Proposal of a cancer cachexia drug discovery cascade focusing on Zinc- α 2-glycoprotein. MSc Thesis, University College London.
- 51 Kumar S & Nussinov R (2002) Close-range electrostatic interactions in proteins. *ChemBioChem* **3**, 604–617.
- 52 Balendiran GK, Schnutgen F, Scapin G, Borchers T, Xhong N, Lim K, Godbout R, Spener F & Sacchettini JC (2000) Crystal structure and thermodynamic analysis of human brain fatty acid-binding protein. *J Biol Chem* **275**, 27045–27054.
- 53 Waku T, Shiraki T, Oyama T, Maebara K, Nakamori R & Morikawa K (2010) The nuclear receptor PPAR γ individually responds to serotonin- and fatty acid-metabolites. *EMBO J* **29**, 3395–3407.
- 54 Cai J, Lucke C, Chen Z, Qiao Y, Klimtchuk E & Hamilton JA (2012) Solution structure and backbone dynamics of human liver fatty acid binding protein: fatty acid binding revisited. *Biophys J* **102**, 2585–2594.
- 55 Teyton L (2018) Role of lipid transfer proteins in loading CD1 antigen-presenting molecules. *J Lipid Res* **59**, 1367–1373.
- 56 Wun KS, Reijneveld JF, Cheng TY, Ladell K, Uldrich AP, Le Nours J, Miners KL, McLaren JE, Grant EJ, Haigh OL *et al.* (2018) T cell autoreactivity directed toward CD1e itself rather than toward carried self lipids. *Nat Immunol* **19**, 397–406.
- 57 Roderick SL, Chan WW, Agate DS, Olsen LR, Vetting MW, Rajashankar KR & Cohen DE (2002) Structure of human phosphatidylcholine transfer protein in complex with its ligand. *Nat Struct Biol* **9**, 507–511.

- 58 Kudo N, Kumagai K, Tomishige N, Yamaji T, Wakatsuki S, Nishijima M, Hanada K & Kato R (2008) Structural basis for specific lipid recognition by CERT responsible for nonvesicular trafficking of ceramide. *Proc Natl Acad Sci USA* **105**, 488–493.
- 59 Jung TW, Park T, Park J, Kim U, Je HD, Kim HD, Cho SW, Abd El-Aty AM, Song JH, Kim HC *et al.* (2019) Phosphatidylcholine causes adipocyte-specific lipolysis and apoptosis in adipose and muscle tissues. *PLoS One* **14**, e0214760.
- 60 Craig LB, Brush RS, Sullivan MT, Zavy MT, Agbaga MP & Anderson RE (2019) Decreased very long chain polyunsaturated fatty acids in sperm correlates with sperm quantity and quality. *J Assist Reprod Genet* **36**, 1379–1385.
- 61 Rival CM, Xu W, Shankman LS, Morioka S, Arandjelovic S, Lee CS, Wheeler KM, Smith RP, Haney LB, Isakson BE *et al.* (2019) Phosphatidylserine on viable sperm and phagocytic machinery in oocytes regulate mammalian fertilization. *Nat Commun* **10**, 4456.
- 62 Jeong HS, Choi HR, Yun HY, Baek KJ, Kwon NS, Park KC & Kim DS (2013) Ceramide PC102 inhibits melanin synthesis via proteasomal degradation of microphthalmia-associated transcription factor and tyrosinase. *Mol Cell Biochem* **375**, 81–87.
- 63 Yang C, Zhang GP, Chen YN, Meng FL, Liu SS & Gong SP (2016) Effects of docosahexaenoic acid on cell apoptosis, invasion and migration of cervical cancer cells in vitro. *Nan Fang Yi Ke Da Xue Xue Bao* **36**, 848–856.
- 64 Gasteiger E, Hoogland C, Gattiker A, Duvaud S, Wilkins MR, Appel RD & Bairoch A (2005) Protein Identification and Analysis Tools on the ExpASY Server. Humana Press, Totowa, NJ.
- 65 Schuck P (1998) Sedimentation analysis of noninteracting and self-associating solutes using numerical solutions to the Lamm equation. *Biophys J* **75**, 1503–1512.
- 66 Schuck P (2000) Size-distribution analysis of macromolecules by sedimentation velocity ultracentrifugation and lamm equation modeling. *Biophys J* **78**, 1606–1619.
- 67 O'Boyle NM, Banck M, James CA, Morley C, Vandermeersch T & Hutchison GR (2011) Open Babel: an open chemical toolbox. *J Cheminform* **3**, 33.
- 68 Trott O & Olson AJ (2010) AutoDock Vina: improving the speed and accuracy of docking with a new scoring function, efficient optimization, and multithreading. *J Comput Chem* **31**, 455–461.
- 69 Wallace AC, Laskowski RA & Thornton JM (1995) LIGPLOT: a program to generate schematic diagrams of protein-ligand interactions. *Protein Eng* **8**, 127–134.
- 70 Notredame C, Higgins DG & Heringa J (2000) T-Coffee: a novel method for fast and accurate multiple sequence alignment. *J Mol Biol* **302**, 205–217.

Supporting information

Additional supporting information may be found online in the Supporting Information section at the end of the article.

Fig. S1. Non-reducing 4–12% SDS-PAGE analysis of Wt and 11 ZAG mutants (excepting ZAG-Y12A).

Fig. S2. AUC sedimentation velocity analyses of Wt and mutant ZAG.

Fig. S3. Fluorescence emission spectra of DAUDA (blue) and C₁₆-BODIPY (red) titrated with the mutant A158G, R157A, E165A and T169A ZAG proteins (black).

Fig. S4. Fluorescence emission spectra of DAUDA (blue) and C₁₆-BODIPY (red) titrated with the mutant L69A, K148A, E79A and E61A ZAG proteins (black).

Fig. S5. Fluorescence emission spectra of DAUDA (blue) and C₁₆-BODIPY (red) titrated with the mutant Y12A, R73A, R73E and R157E ZAG proteins (black).

Fig. S6. Fluorescence emission spectra of 1.3 μM DAUDA and 1.3 μM C₁₆-BODIPY upon addition with 12 μM DHA, 12 μM PC, 12 μM ceramide and 12 μM DAG.

Fig. S7. Fluorescence emission spectra of 1.3 μM DAUDA and 1.3 μM C₁₆-BODIPY upon addition with 12 μM PS, 12 μM sphingomyelin and 12 μM C32:6 fatty acid.

Fig. S8. Denaturing liquid chromatography mass spectrometry of ZAG and ZAG: lipid complexes.

Fig. S9. ICP-QMS analysis of zinc concentrations in ZAG and four mutant proteins in 10 mM HEPES, pH = 7.2.

Table S1. Crystallographic ligands of CD1a, CD1b, CD1c and CD1d docked to the ZAG groove.